J. Fluid Mech. (2015), *vol.* 766, *pp.* 405–435. © Cambridge University Press 2015
doi:10.1017/jfm.2015.18

Optimal wavepackets in streamwise corner flow

Oliver T. Schmidt[1,†], Seyed M. Hosseini[2], Ulrich Rist[1], Ardeshir Hanifi[2,3] and Dan S. Henningson[2]

[1]Institut für Aerodynamik und Gasdynamik, Universität Stuttgart, D-70569 Stuttgart, Germany

[2]Linné Flow Center and Swedish e-Science Research Centre (SeRC), KTH Mechanics, SE-100 44 Stockholm, Sweden

[3]Swedish Defence Research Agency, FOI, SE-164 90 Stockholm, Sweden

(Received 19 May 2014; revised 17 November 2014; accepted 8 January 2015)

The global non-modal stability of the flow in a right-angled streamwise corner is investigated. Spatially confined linear optimal initial conditions and responses are obtained by use of direct-adjoint looping. Two base states are considered, the classical self-similar solution for a zero streamwise pressure gradient, and a modified solution that mimics leading-edge effects commonly observed in experimental studies. The latter solution is obtained in a reverse engineering fashion from published measurement data. Prior to the global analysis, a classical local linear stability and sensitivity analysis of both base states is conducted. It is found that the base-flow modification drastically reduces the critical Reynolds number through an inviscid mechanism, the so-called corner mode. A survey of the geometry of the two base states confirms that the modification greatly aggravates the inflectional nature of the flow. Global optimals are calculated for subcritical and supercritical Reynolds numbers, and for two finite optimization times. The optimal initial conditions are found to be self-confined in the spanwise directions, and symmetric with respect to the corner bisector. They evolve into streaks or streamwise modulated wavepackets, depending on the base state. Substantial transient growth caused by the Orr mechanism and the lift-up effect is observed.

Key words: absolute/convective instability, boundary layer stability, boundary layers

1. Introduction

Linear optimal initial conditions for the flow in an axial corner are considered. The classical corner-flow problem, as sketched in figure 1, consists of two right-angled, semi-infinite flat plates with the potential flow u_∞ aligned with the intersection line. Here, x denotes the streamwise direction, and the two spanwise coordinates y and z span the transversal plane. In addition, a 45°-rotated, auxiliary coordinate system is introduced with its abscissa s along the corner bisector. A set of equations based on the Blasius similarity transformation and matched asymptotic expansions, the so-called corner-flow equations, was derived by Rubin (1966). They describe the laminar, incompressible flow in the transversal corner plane and were first solved numerically by Rubin & Grossman (1971). As far-field boundary conditions, the authors relied

† Email address for correspondence: o.schmidt@iag.uni-stuttgart.de

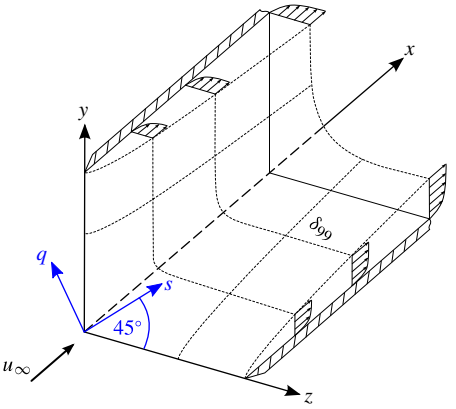

FIGURE 1. (Colour online) Sketch of the flow in a streamwise corner (Schmidt & Rist 2011).

on the solution of an additional set of equations governing the asymptotic secondary cross-flow induced by the superposition of the displacement effects of the two plates (Pal & Rubin 1971). Detailed overviews of many numerical corner-flow studies can be found in the works of Ridha (2003), Galionis & Hall (2005) and Schmidt & Rist (2011). The topics include the effects of compressibility (Weinberg & Rubin 1972), a non-zero streamwise pressure gradient (Ridha 1992) and arbitrary corner angles (Barclay & Ridha 1980). The main difficulty in corner-flow computations stems from the observation that the influence of the corner on the cross-flow field does not decay exponentially with increasing distance from the intersection line. Consequently, either a sufficiently large computational domain has to be chosen or a coordinate transform that maps the far-field boundaries to true infinity as realized by Ghia (1975) and Mikhail & Ghia (1978) has to be applied.

Numerous linear stability analyses based on the self-similar corner-flow solutions mentioned above have been conducted in the past, starting with studies of one-dimensional velocity profiles of the blending boundary layer between the corner region and the asymptotic far-field solution by Lakin & Hussaini (1984), Dhanak (1992, 1993) and Dhanak & Duck (1997). The two-dimensional linear stability problem for the self-similarity solution was first addressed by Balachandar & Malik (1995) within an inviscid framework. The effect of a streamwise pressure gradient was included in the viscous corner-flow stability study by Parker & Balachandar (1999), the influence of compressibility in Schmidt & Rist (2011) and the spatial non-parallel stability problem was examined by Galionis & Hall (2005) and Alizard, Rist & Robinet (2009) by solving the parabolized stability equations.

Despite the different approaches taken, a major inconsistency between numerical studies and experimental surveys remains unsolved. While linear stability analyses of the self-similar base state predict a critical Reynolds number of $Re_{x,c} \approx 9 \times 10^4$ (Balachandar & Malik 1995; Parker & Balachandar 1999; Galionis & Hall 2005; Schmidt & Rist 2011), experimental evidence suggests a transitional Reynolds number as low as $Re_{x,c} \approx 10^4$ (even for a small favourable pressure gradient). Experimental data from more than two decades starting with early measurements by Nomura (1962) was collected and compared with each other and with theory by Zamir (1981). The reader is referred to this comprehensive aggregation of data for an insight into the experimental evidence. A major point of discussion is the validity of the self-similarity

solution as measurements commonly show a deviation from the theoretical laminar flow in the near-corner region. Kornilov & Kharitonov (1982) attributed the deviation to the pressure field induced by the intersection of the plates in the leading-edge region in their experimental study.

Balachandar & Malik (1995) explained the discrepancy between experiment and theory by the presence of an inviscid mechanism in the corner region. They found a critical Reynolds number of $Re_{x,c} = 435$ for the one-dimensional bisector-profile instability but could not confirm this number for the two-dimensional problem. A nonlinear mechanism was brought into the discussion as a possible cause by Galionis & Hall (2005). Only recently, Alizard, Robinet & Rist (2010) computed the sensitivity of the self-similar corner-flow solution with respect to base-flow variations and suggested a transient growth mechanism to explain the low transitional Reynolds number. In this paper, we follow that route and assess the question of how much kinetic energy a localized perturbation can maximally gain from the mean flow while being advected downstream over some finite time τ. This is done by computing global optimal initial conditions that are artificially restricted to a finite streamwise extent. A time-stepper-based optimization technique, as introduced by Monokrousos *et al.* (2010) for the computation of optimal solutions for flat plate boundary layer, is employed for that purpose. The artificial localization of the optimal initial condition is a numerical necessity caused by the spatial inhomogeneity of the base flow. The resulting response manifests in form of a wavepacket. The use of optimization techniques to calculate optimal perturbations in fluid dynamic applications dates back to Farrell (1988), who calculated the optimal excitation in constant shear flow, first in two and later in three dimensions (Butler & Farrell 1992; Farrell & Ioannou 1993). The authors found three-dimensional optimal structures which exhibit large energy growth despite the absence of unstable normal modes. Two already known mechanisms were identified as the main causes of non-modal growth. First, the Orr mechanism (Orr 1907; Lindzen 1988) that allows perturbation waves whose fields of constant phase are initially inclined against the mean shear to extract energy from the base flow by adopting to the mean shear while being convected downstream. Second, the lift-up mechanism as described by Ellingsen & Palm (1975) and Landahl (1975, 1980). It describes the generation of streamwise streaks caused by momentum transfer from vortical structures in the cross-flow plane to the streamwise velocity component. The lift-up of a low-speed streak leads to an inflection point in the streamwise velocity profile and, hence, gives rise to an inviscid instability of secondary nature. The Orr and the lift-up mechanisms were identified by Monokrousos *et al.* (2010) on the flat plate as the origin of transient growth for long and short optimization times, respectively. In recent work by Alizard, Robinet & Guiho (2012), the authors investigated the non-modal behaviour of the self-similar corner-flow solution within a parallel framework, and found that the same two effects lead to substantial transient growth. The maximum gain was achieved by optimal structures that are antisymmetric with respect to the corner bisector. In a direct numerical simulation (DNS) conducted by Schmidt & Rist (2014), it was found that corner flow is prone to spatial transient growth under harmonic forcing at subcritical Reynolds numbers. It was demonstrated that pseudo-resonance between the inviscid corner mode and viscous branch solutions causes a moderate transient perturbation amplification. The present study elaborates on the non-modal worst-case scenario in form of linear global optimal perturbations. The results are put in the context of the last mentioned DNS findings, the computations by Alizard *et al.* (2010, 2012) and the investigation of the related flat-plate flow by Monokrousos *et al.* (2010). In fact, the present work can be regarded as a continuation

of the aforementioned studies: the transient growth study by Alizard *et al.* (2012) is extended by incorporating non-parallel effects, and the survey on optimal disturbances by Monokrousos *et al.* (2010) by considering a fully three-dimensional base state, i.e. without homogeneity in the spanwise direction.

The paper is organized as follows: the governing equations and theoretical concepts are introduced in § 2. Subsequently, their numerical implementation is explained in § 3. The main part of the paper consists of the presentation and interpretation of the results of the global non-modal study in § 4. Prior to this, the two base states are presented and a classical local stability and sensitivity analysis is conducted. The paper ends with a summary of the results and a comparison with previous literature in § 5.

2. Theoretical background

The governing equations and their linearized counterpart are presented in § 2.1. Under the assumption of infinitesimally small wave-like perturbations, the eigenvalue problem (EVP) of classical linear stability theory is obtained in § 2.2. The ϵ-pseudospectrum-based sensitivity analysis of linear operators is recapitulated in the same section. Finally, the theory of global linear optimals which is at the basis of the present study is addressed in § 2.3.

2.1. *Governing equations*

The motion of an incompressible fluid in a domain $\mathscr{D}$ is governed by the incompressible Navier–Stokes equations supplemented by the continuity equation

$$\frac{\partial \boldsymbol{u}}{\partial t} = -(\boldsymbol{u}\cdot\boldsymbol{\nabla})\,\boldsymbol{u} - \boldsymbol{\nabla} p + \frac{1}{Re}\nabla^2\boldsymbol{u}, \quad \boldsymbol{\nabla}\cdot\boldsymbol{u} = 0 \ \text{ in } \mathscr{D}, \tag{2.1}$$

where $\boldsymbol{u}(\boldsymbol{x},\, t) = [u\ v\ w]^{\mathrm{T}}\,(x,\, y,\, z,\, t)$ is the vector of Cartesian velocity components and $p(x,\, y,\, z,\, t)$ the pressure. Here $Re = u_\infty \delta/\nu$ is the Reynolds number based on some characteristic length δ, the far-field velocity u_∞ and the kinematic viscosity ν. Velocities are non-dimensionalized by u_∞, Cartesian coordinates by δ, and a unit density is assumed. Here, we choose $\delta \equiv \delta^*(x_0)$, where $\delta^* = \int_0^\infty (1 - U/u_\infty)\mathrm{d}y$ is the displacement thickness of the one-dimensional far-field velocity profile which coincides with the classical Blasius boundary layer solution for the streamwise and wall-normal velocity components. Here x_0 refers to the start of the computational domain. The Navier–Stokes equations (2.1) can be linearized by Reynolds decomposing the velocity and pressure fields into a steady base flow $\{\boldsymbol{U}(\boldsymbol{x}),\ \ P(\boldsymbol{x})\}$, which is a solution to (2.1) itself, and a small perturbation $\epsilon\{\boldsymbol{u}'(\boldsymbol{x},\, t),\ p'(\boldsymbol{x},\, t)\}$, i.e. $\boldsymbol{u} = \boldsymbol{U} + \epsilon\boldsymbol{u}'$, and $p = P + \epsilon p'$. The linearized Navier–Stokes equations

$$\frac{\partial \boldsymbol{u}'}{\partial t} = -(\boldsymbol{U}\cdot\boldsymbol{\nabla})\boldsymbol{u}' - \left(\boldsymbol{u}'\cdot\boldsymbol{\nabla}\right)\boldsymbol{U} - \boldsymbol{\nabla} p' + \frac{1}{Re}\nabla^2\boldsymbol{u}', \quad \boldsymbol{\nabla}\cdot\boldsymbol{u}' = 0 \ \text{ in } \mathscr{D} \tag{2.2}$$

are obtained by keeping only terms that are linear in the bookkeeping variable ϵ or, equivalently, by neglecting products of small quantities. Problem-dependant boundary conditions are enforced on the boundaries $\partial\mathscr{D}$.

2.2. *Local linear stability theory*

In classical local linear stability theory, wave-like (normal-mode) solutions of the form $\boldsymbol{q}'(y,\, z,\, t) = \hat{\boldsymbol{q}}(y,\, z)\,\mathrm{e}^{\mathrm{i}(\alpha x - \omega t)}$ upon a parallel laminar base-state $\boldsymbol{Q}(y,\, z)$ are considered,

where $\boldsymbol{q}'$ and $\boldsymbol{Q}$ represent the solution vector of perturbation flow quantities and the corresponding base-state, respectively. Inserting the normal-mode ansatz in (2.2) gives an EVP for the amplitude function $\hat{\boldsymbol{q}}$ with the complex streamwise wavenumber $\alpha \in \mathbb{C}$ as the corresponding eigenvalue. Here, we let $\omega \in \mathbb{R}$ as we are interested in the spatial evolution of a harmonic wave at a given forcing frequency ω, i.e. in spatial stability. Spatial amplification is found for $\mathrm{Im}\{\alpha\} < 0$. The resulting spatial linear stability EVP can be written in matrix (discretized) form as $(\boldsymbol{L}_0 + \alpha \boldsymbol{L}_1 + \alpha^2 \boldsymbol{L}_2)\hat{\boldsymbol{q}} = 0$, and is of second order in the eigenvalue α. Most commonly, the second-order EVP is reduced to an extended linear EVP

$$\left(\widetilde{\boldsymbol{L}}_0 + \alpha \widetilde{\boldsymbol{L}}_1\right) \tilde{\boldsymbol{q}} = 0 \tag{2.3}$$

through the introduction of a set of auxiliary variables $\tilde{\boldsymbol{q}} = [\hat{\boldsymbol{q}}\ \alpha\hat{\boldsymbol{q}}]^{\mathrm{T}}$. The reader is referred to the reviews by Mack (1984) and Theofilis (2003) for details on the subject.

The classical eigenvalue-based analysis outlined above describes the long-time response by considering the dominant eigenvalue of the linear system. For non-normal operators, however, significant (short-time) transient growth can occur as a result of the non-orthogonality of the solution space spanned by the eigenvectors (Reddy, Schmid & Henningson 1993; Trefethen *et al.* 1993). The sensitivity of the spectrum to generally random perturbations to the governing linear operator can be quantified in terms of ϵ-pseudospectra as shown by Trefethen (1991). The reader is referred to the latter three references for details. By definition, a complex number $\alpha \in \mathbb{C}$ is said to be in the ϵ-pseudospectrum if

$$\|(\alpha \widetilde{\boldsymbol{L}}_1 - \widetilde{\boldsymbol{L}}_0)^{-1}\|_E \geqslant \frac{1}{\epsilon}, \tag{2.4}$$

where $(\alpha \widetilde{\boldsymbol{L}}_1 - \widetilde{\boldsymbol{L}}_0)^{-1}$ is the resolvent and $\|\cdot\|_E$ some appropriate energy norm. For incompressible flows, the perturbation kinetic energy in form of the standard Euclidean 2-norm $\|\hat{\boldsymbol{u}}\|_2$ is chosen. The contours of the resolvent for some value ϵ can be interpreted as the upper bound for the eigenvalues of a randomly perturbed operator $\widetilde{\boldsymbol{L}}_0 + \boldsymbol{E}$, where $\boldsymbol{E}$ is a random matrix of norm $\|\boldsymbol{E}\|_E \leqslant \epsilon$.

2.3. *Global optimal disturbances*

Within the framework of optimal initial conditions we are interested in finding a solution to (2.2), possibly subject to other constraints, that maximizes some measure of energy while evolving over a finite time span $t \in [0, \tau]$. To do so, we first introduce the concept of a linear evolution operator $\mathscr{A}(t)$ that maps an initial perturbation $\boldsymbol{u}'(t_0)$ to $\boldsymbol{u}'(t + t_0)$ at some other time instant, i.e. $\boldsymbol{u}'(t + t_0) = \mathscr{A}(t)\boldsymbol{u}'(t_0)$. Further, we use the standard L_2 inner product $\langle \boldsymbol{u}, \boldsymbol{v} \rangle = \int_{\mathscr{D}} \boldsymbol{u} \cdot \boldsymbol{v} \mathrm{d}\mathscr{D}$, which conveniently defines the norm associated with the kinetic energy of the perturbation $\|\boldsymbol{u}'\|_2 = \langle \boldsymbol{u}', \boldsymbol{u}' \rangle$. As we are interested in the transient development of an initial perturbation, we first have to define a suitable measure of such, i.e. transient growth. The term refers to the ratio of the perturbation kinetic energy normalized by its initial condition at $t = 0$ (Reddy & Henningson 1993; Trefethen *et al.* 1993), and can be recast in terms of the linear evolution operator as follows:

$$G(t) \equiv \frac{E(t)}{E(0)} = \frac{\|\boldsymbol{u}'(t)\|_2}{\|\boldsymbol{u}'(0)\|_2} = \frac{\langle \mathscr{A}(t)\boldsymbol{u}'(0), \mathscr{A}(t)\boldsymbol{u}'(0) \rangle}{\langle \boldsymbol{u}'(0), \boldsymbol{u}'(0) \rangle} = \frac{\left\langle \boldsymbol{u}'(0), \mathscr{A}^\dagger(t)\mathscr{A}(t)\boldsymbol{u}'(0) \right\rangle}{\langle \boldsymbol{u}'(0), \boldsymbol{u}'(0) \rangle}. \tag{2.5}$$

Here, the action of the adjoint operator $\mathscr{A}^\dagger$ is given by

$$\left\langle \mathscr{A}\boldsymbol{u}', \boldsymbol{u}^\dagger \right\rangle = \left\langle \boldsymbol{u}', \mathscr{A}^\dagger \boldsymbol{u}^\dagger \right\rangle. \tag{2.6}$$

By looking for the solution that maximizes the transient growth over some finite time τ we define the maximum growth $G_{max}(\tau)$ as

$$G_{max}(\tau) \equiv \max_{\|\boldsymbol{u}'(0)\|\neq 0} \frac{E(\tau)}{E(0)} = \max_{\|\boldsymbol{u}'(0)\|\neq 0} \frac{\left\langle \boldsymbol{u}'(0), \mathscr{A}^{\dagger}(\tau)\mathscr{A}(\tau)\boldsymbol{u}'(0)\right\rangle}{\langle \boldsymbol{u}'(0), \boldsymbol{u}'(0)\rangle}. \tag{2.7}$$

From (2.7), note that the last term in the equality corresponds to the induced matrix norm of $\mathscr{A}^{\dagger}(\tau)\mathscr{A}(\tau)$. Hence, the dominant eigenvalue of $\mathscr{A}^{\dagger}(\tau)\mathscr{A}(\tau)$ (or singular value of $\mathscr{A}(\tau)$, respectively) is the solution to the optimization problem (2.7).

The linear evolution operator $\mathscr{A}(\tau)$ and its adjoint counterpart cannot be formulated directly without the assumption of local eigenfunctions (Luchini 2000). However, the action of the evolution operator on an initial perturbation can be obtained from integrating the underlying initial value problem. From that perspective, the linear operator defined by (2.2) acts as the infinitesimal generator of the evolution operator $\mathscr{A}(\tau)$ (Edwards *et al.* 1994). The action of the adjoint evolution operator $\mathscr{A}^{\dagger}(\tau)$ can be approximated in the same manner by integration of the adjoint equations corresponding to the linearized Navier–Stokes equations (2.2)

$$-\frac{\partial \boldsymbol{u}^{\dagger}}{\partial t} = -(\boldsymbol{U}\cdot\nabla)\boldsymbol{u}^{\dagger} + (\nabla \boldsymbol{U})^{\mathrm{T}}\cdot\boldsymbol{u}^{\dagger} - \nabla p^{\dagger} + \frac{1}{Re}\nabla^2\boldsymbol{u}^{\dagger}, \quad \nabla\cdot\boldsymbol{u}^{\dagger} = 0 \ \text{ in } \mathscr{D}. \tag{2.8}$$

Equations (2.8) are derived by substituting the linear operator defined by (2.2) into the left-hand side of (2.6), then integrating by parts the individual terms and subsequently recasting the equation in form of the inner product on the right-hand side of (2.6). Now note that applying $\mathscr{A}^{\dagger}(\tau)$ to $\mathscr{A}(\tau)\boldsymbol{u}'(0)$ in (2.7) corresponds to taking $\boldsymbol{u}'(\tau)$ as the initial condition for integrating the adjoint linearized Navier–Stokes equations (2.8). Together with the observation that (2.8) features a negative sign in front of the time derivative term, we see that the action of $\mathscr{A}^{\dagger}(\tau)$ evolves the initial perturbation backwards in time. A detailed derivation of the adjoint evolution operator and the adjoint Navier–Stokes equations can be found in Bagheri, Brandt & Henningson (2009).

3. Numerical methods

In the following, the numerical methods used for the calculation of the laminar base-states, the spatial local stability and sensitivity analysis and the global optimization are described in §§ 3.1–3.3, respectively.

3.1. *Self-similar base-state calculation*

Two laminar base states are considered in this study: the canonical self-similar solution as first obtained by Rubin (1966) and used throughout literature, and an altered base-flow that better imitates experimental results. The canonical state is henceforth referred to as non-modified or zero pressure gradient (ZPG), and the second referred to as the modified base flow. The latter mimics the bulge-shaped deformation in the near-corner region as observed in experimental studies. Here, measurement data taken from the study by Zamir & Young (1970) serves as a reference. The exact form of the deformation depends on the leading-edge geometry and is a function of the position along the plates. Therefore, it renders the base-state non-self-similar and cannot be modelled accurately without taking into account the fully three-dimensional nature of the leading-edge flow, which is beyond the scope

of this study. However, given the experimental reference, a body force term (or, equivalently, streamwise pressure gradient term) can be constructed that deforms the self-similar base-state in the desired manner. Both laminar base states are obtained as solutions to the parabolized Navier–Stokes (PNS) equations. Under the assumption of a steady laminar flow with negligible upstream effects, the fundamental equations can be simplified significantly, and be solved by a downstream space-marching procedure (see e.g. Tannehill, Anderson & Pletcher 1997). We employ the same code as used and validated in Schmidt & Rist (2011). The procedure used to converge self-similar base states employed in the present work is also described therein, as well as the computation strategy for the one-dimensional far-field solution required for the far-field boundary condition. The latter is based on the solution of a designated equation for the asymptotic secondary cross-flow profile (Ghia & Davis 1974) as described in more detail in Schmidt & Rist (2014). The so-obtained profile corresponds to the lower branch (Blasius-like) of the dual solution in the work of Ridha (1992), who showed that two solutions to the incompressible corner-flow equations exist, even for a zero streamwise pressure gradient. It is the only solution permitted by our framework, and almost exclusively used throughout literature. The code shares the same Chebyshev-collocation-based spatial differentiation scheme with the linear stability code, and utilizes a first-order accurate implicit Euler method to advance the solution in the streamwise direction. The code is used as is for the calculation of the canonical ZPG solution.

For the calculation of the modified base state which mimics the bulge-shaped deformation, however, a code modification is required. We aim at reproducing the general effect of the deformation on stability by taking a reverse-engineering approach. First, a two-dimensional streamwise velocity field featuring the bulge deformation is reconstructed by interpolation and extrapolation of published hot-wire measurement data. Second, the latter field data is transformed into self-similar (Levy–Lees) coordinates and the difference to the self-similar solution, here termed ΔU, is sought. Third, ΔU is used within a body forcing term (or, equivalently, a localized streamwise pressure gradient) to obtain a self-similar base state featuring the same deformation. Self-similarity of the result is achieved by assuming a force term that is compatible with the well-known Falkner–Skan similarity transformation, i.e. to a viscous boundary-layer-type flow with a potential far-field solution that satisfies $U(x) = u_\infty x^m$. The sign of the exponent m determines whether the flow is accelerated ($m > 0$) or retarded ($m < 0$). For the flat-plate solution, boundary-layer separation occurs for $m \leqslant -0.091$. Note that unlike for Falkner–Skan flow, ΔU has compact support in our procedure as the interpolated experimental solution approaches the self-similar base state at some distance away from the close-corner region. In addition, we assume that the asymptotic corner-flow solution enforced on the far-field boundaries is valid for the forced model as well, i.e. that the outer boundaries are sufficiently far away from the region of influence of the forcing. In operator notation, the PNS system can be written compactly as

$$\boldsymbol{P}\boldsymbol{Q}^{(i+1)} = \boldsymbol{r} + c\Delta\boldsymbol{Q}mx^{2m-1}. \tag{3.1}$$

Here, $\boldsymbol{P}$ is the discretized PNS operator, and the self-similar forcing term is added to the right-hand side $\boldsymbol{r}$ of the equation. For self-similarity, the forcing term must be of the same form as the streamwise pressure gradient equivalent to the above-mentioned potential flow distribution. A factor c is introduced for the adjustment of the amplitude. The solution vector and the body force distribution

Base-state	n_{Re}	n_ω	N_y	N_z	ω_0	ω_1	$Re_{x,0}$	$Re_{x,1}$	y_1	z_1
ZPG	45	15	45	45	0.03	0.15	85×10^3	5×10^5	35	35
Modified	60	15	45	45	0.03	0.15	5×10^3	5×10^5	35	35

TABLE 1. Parameters of the spatial local stability calculation. Here n_{Re} and n_ω are the number of data points along the Reynolds number and frequency axis, respectively. Here N_y and N_z are the number of Gauss–Lobatto points in the spanwise directions.

vector are given by $\boldsymbol{Q} = [\rho\ U\ V\ W\ T]^{\mathrm{T}}$ and $\Delta\boldsymbol{Q} = [0\ \Delta U\ 0\ 0\ 0]^{\mathrm{T}}$, respectively. The density ρ and temperature T are part of the solution as the solver is written for a general compressible fluid. Incompressible limit solutions are obtained by considering the low-Mach-number regime, i.e. by setting $Ma = 0.1$ for the case at hand. The temperature and density solution are omitted henceforth. The validity of the procedure is confirmed *a posteriori*: fully converged self-similar solutions were obtained for a range of amplitude factors c and exponents m. A satisfactory fit to the reference solution as presented later in § 4.1 was obtained for $m = -0.05$ and $c = 2$. The results presented in § 4.1 are obtained on a 50×50 collocation point grid to resolve a domain of size $y, z \in [0, 0] \times [50, 50]$. The large domain extent guarantees the validity of the asymptotic far-field solution, even for the modified base-state calculation. As in Schmidt & Rist (2011), a fast convergence towards a self-similar state was observed.

3.2. *Spatial local stability calculation*

The spatial local stability EVP (2.3) is solved by a shift-and-invert Arnoldi algorithm on a transformed Chebyshev-collocation grid as in Schmidt & Rist (2011). A spatial resolution of 45×45 collocation points is used to resolve a domain of size $y, z \in [0, 0] \times [35, 35]$, where the walls are situated at $y = 0$ and $z = 0$, respectively. The spanwise coordinates are normalized by the local displacement thickness of the far-field solution. An algebraic grid stretching is applied to cluster half of the points in the wall-near 20 % of the domain along both walls. The 15 leading (usually 14 viscous Tollmien–Schlichting-type modes and the inviscid corner mode) modes are converged to a tolerance of $\sigma = 10^{-6}$ for each (Re_x, ω) combination. For the construction of the stability diagrams in § 4.1, the frequency domain is resolved by 15 equally spaced points. Along the abscissa a resolution of 45 and 60 points is chosen for the ZPG and the modified base state, respectively. Table 1 summarizes the parameters used for the linear stability calculations presented in § 4.2. The efficient routines of the EigTool library (Wright 2002) are employed to calculate the resolvent in (2.4) in the context of eigenvalue sensitivity.

3.3. *Global optimal disturbances with Nek5000*

The actions of the linear evolution operator $\mathscr{A}$ and its adjoint $\mathscr{A}^\dagger$ are calculated by time integration of the linear direct and linear adjoint Navier–Stokes equations, (2.1) and (2.8), respectively. Both sets of equations are solved with the spectral element code Nek5000 (Fischer, Lottes & Kerkemeier 2008) that was also used in the reference study by Monokrousos *et al.* (2010). It uses semi-implicit time-stepping combined with a weighted residual spectral element method (Patera 1984) for the spatial discretization. For this study, we choose to combine second-order-accurate time-stepping with spectral elements of a polynomial order of 7, and solve the

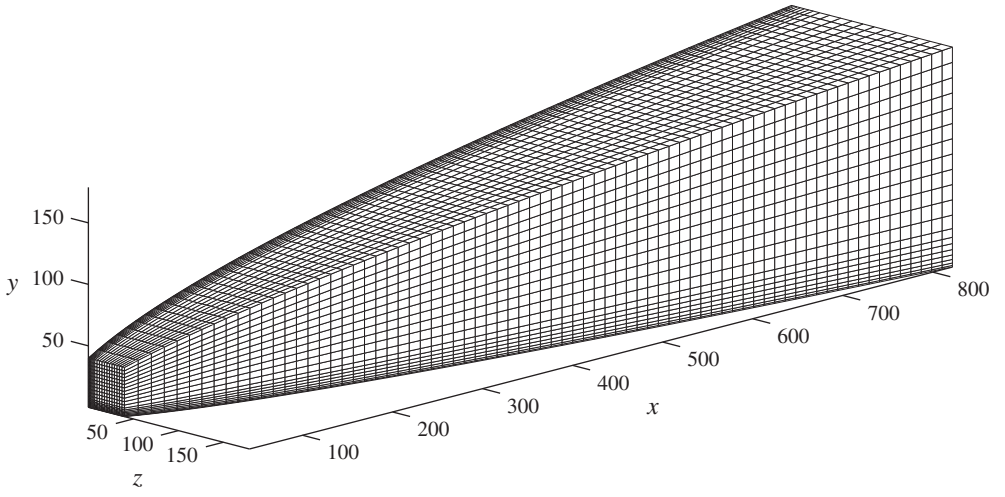

FIGURE 2. Isometric view of the Nek5000 computational grid for the low-Reynolds-number case. The domain height corresponds to $45\delta^*(x)$. Only every second grid line is shown for clarity.

Case name	N	n_x	n_y	n_z	Re_0	Re_1	$Re_{x,0}$	$Re_{x,1}$	$y_1\dfrac{\delta^*(x_0)}{\delta^*(x)}$	$z_1\dfrac{\delta^*(x_0)}{\delta^*(x)}$
low-*Re*	7	150	41	41	121.7	544.2	5×10^3	100×10^3	45	45
high-*Re*	7	150	41	41	632.3	825.3	135×10^3	230×10^3	45	45

TABLE 2. Computational domains for the direct and adjoint Navier–Stokes simulations. Here N is the polynomial order for the velocity field approximation and n_x, n_y, and n_z the number of grid points in the Cartesian directions.

governing equations in the $\mathbb{P}_N$–$\mathbb{P}_{N-2}$ formulation. The notation suggests that the velocity field is approximated by Nth-order Lagrangian interpolants on Gauss–Lobatto–Legendre points, and the pressure field by $(N-2)$th-order interpolants on interior Gauss–Legendre nodes. Two computational grids are constructed, one for the low-Reynolds-number case, and one for the high-Reynolds-number case, respectively. Both share the same spatial resolution of $150\times41\times41$ grid blocks, and the same size in self-similar coordinates, i.e. a domain height corresponding to $45\delta^*(x)$ and the same (dimensional) length. The grid for the low-Reynolds-number case is shown in figure 2. It can be seen that clustering towards the near-wall region has been applied for a proper resolution of the boundary layer. In the streamwise direction, the grid is uniform. At the given polynomial order of $N=7$, the grid amounts to a total of $\approx87\times10^6$ degrees of freedom per velocity variable and $\approx33\times10^6$ for the pressure. Details on the two computational domains are provided in table 2.

In § 2.3, we noted that the initial perturbation that maximizes transient growth corresponds to the dominant eigenvector of $\mathscr{A}^\dagger(\tau)\mathscr{A}(\tau)$. Therefore, the optimal initial perturbation is most easily obtained by means of power iterations of the form $\boldsymbol{u}'(0)^{k+1}=\mathscr{A}^\dagger(\tau)\mathscr{A}(\tau)\boldsymbol{u}'(0)^k$, as in the pioneering works by Andersson, Berggren & Henningson (1999), Corbett & Bottaro (2000) and Luchini (2000). We define a convergence criterion through the residual of two consecutive iteration steps in terms

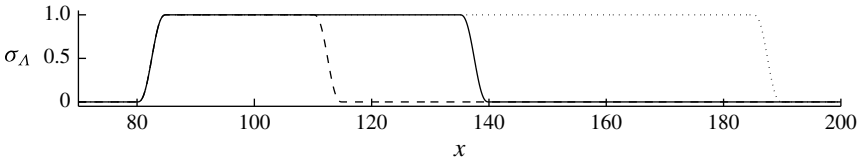

FIGURE 3. Windowing functions over the streamwise coordinate for the low-*Re* computational domain: short (——), intermediate (- - - -) and long (· · · · · ·). The intermediate case is our standard, while the other two cases are used for comparison in § 4.3.1.

of the energy norm $\|\boldsymbol{u}'(0)^k - \boldsymbol{u}'(0)^{k-1}\|_2 \leqslant \epsilon$, where ϵ is the convergence tolerance and superscript k denotes the iteration level. Upon convergence, $\boldsymbol{u}'(0)^k$ approximates the optimal initial condition sought after. We are interested in an optimal initial perturbation that is restricted to some streamwise area $\Lambda \subset \mathscr{D}$ of the computational domain. This adds an additional constraint to the optimization problem (2.7). In practice, the localization is realized by multiplying the adjoint solution at $t = 0$ with a windowing function $\sigma_\Lambda(x)$ that is zero everywhere except within some streamwise region as depicted in figure 3. In order to prevent a discontinuity in the initial perturbation, the windowing function is smoothly ramped following a fifth-order polynomial distribution over a streamwise distance of $\Delta x = 5$ on both sides. Note that no artificial localization is applied in the spanwise directions. As initial perturbation $\boldsymbol{u}'(0)^1$, we chose a wavepacket generated by a spherical volume force acting on the streamwise momentum component in the time interval $t \in [0, 30]$, centred in the middle of the confinement region in the streamwise direction and on the corner bisector in the transversal plane. The resulting initial perturbation is symmetric and hence greatly facilitates the convergence of a symmetric optimal perturbation. A random and an antisymmetric initial perturbation were also tested. Both resulted in a much slower convergence rate, but towards the same symmetric optimal. It is important to stress that not even an antisymmetric initialization gave an antisymmetric optimal result. As it seems, even the smallest numerical error is picked up by the power iteration procedure to produce the dominant symmetric optimal as final result.

The overall optimal initial perturbation algorithm looks as follows. Starting from some initial perturbation $\boldsymbol{u}'(0)^1$, the kth iteration reads:

(*a*) integrate the forward Navier–Stokes system (2.2) with $\boldsymbol{u}'(0)^{k-1}$ as the initial condition to obtain $\boldsymbol{u}'(\tau)^k$;

(*b*) integrate the adjoint Navier–Stokes system (2.8) with $\boldsymbol{u}'(\tau)^k$ as the initial condition to obtain $\boldsymbol{u}'(0)^k$;

(*c*) localize the perturbation to the subspace Λ by applying a windowing function σ_Λ and normalize solution to $\|\boldsymbol{u}'(0)^k\|_2 = 1$;

(*d*) check the convergence criterion and go back to (*a*) with $k \to k + 1$ if it is not met.

Successive initial velocity field iterates can be scaled to unity perturbation kinetic energy as done in (*c*) without loss of generality within the linear framework. A detailed derivation of the constrained optimization problem using Lagrange multipliers can be found in the article by Monokrousos *et al.* (2010).

As examples of the convergence of the direct-adjoint looping, two cases sharing the same Reynolds number and optimization time but with different localization widths are considered in figure 4. Convergence is judged in terms of the transient

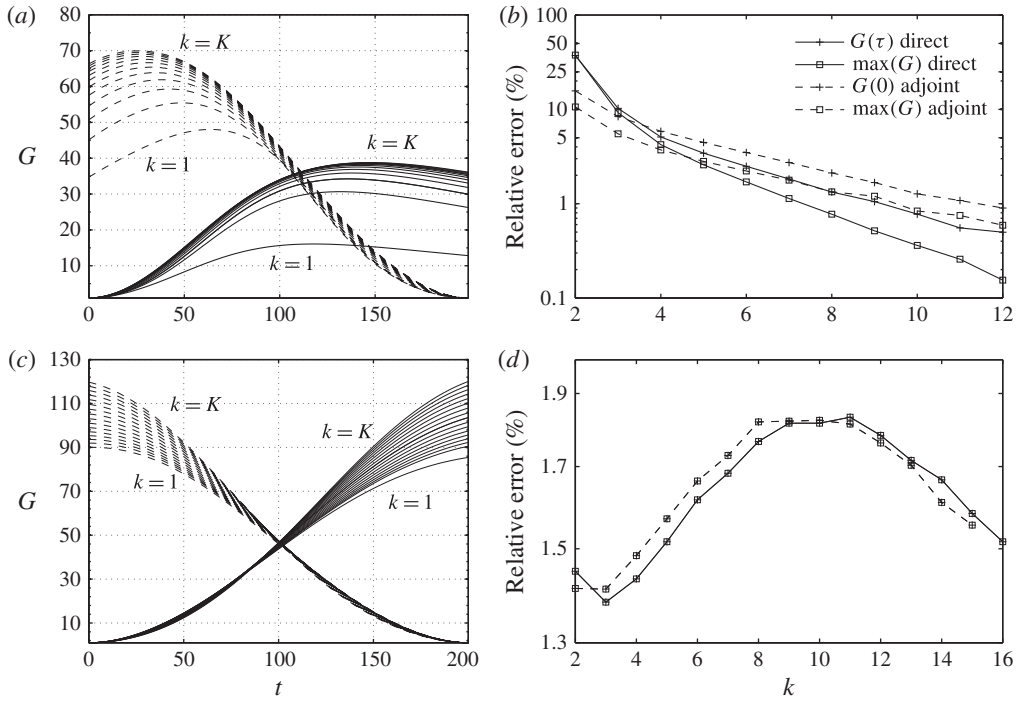

FIGURE 4. Convergence of the direct-adjoint looping for the ZPG base state in the low-*Re* regime and $\tau = 200$: (*a*,*b*) short windowing width; (*c*,*d*) no windowing. Here G is the transient energy growth as defined in (2.5) and k the iteration count. The relative error is calculated as the difference between two successive iterations normalized by the value at the final iteration K, e.g. $(G(\tau)^k - G(\tau)^{k-1})/G(\tau)^K$ for the direct sweep and $G = G(\tau)$.

energy evolution and the relative error of the latter between successive iterations. In figure 4(*a*,*b*) the short windowing extent is considered. It can be seen how the growth curves rapidly converge towards the final optimal solution. An exponential decrease of the relative error can be seen for both, the direct and the adjoint sweeps. No windowing, i.e. $\sigma_\Lambda = 1$, is applied in the second case depicted in figure 4(*c*,*d*). This example clearly demonstrates why the localization is a numerical necessity in the present setup. The relative error between iterations does not drop monotonically and no convergence is to be expected as the perturbation is limited only by the computational domain extent. This is supported by the observation that the optimal structure grows from step to step. For all optimal solutions presented in the following work, a monotonic decrease of the error below 2 % in all four quantities, and the convergence of the optimal structures is ensured. As expected, an even faster convergence as in the example shown in figure 4(*a*,*b*) above is observed for unstable flows, i.e. high-*Re* and modified base-state cases.

4. Results

First, the two base-states are introduced with a special focus on the differences between the ZPG and the modified solutions in § 4.1. The two base flows are subsequently analysed by means of classical local stability theory in § 4.2. In addition, the sensitivity of the underlying linear operator is considered. Finally, the results of

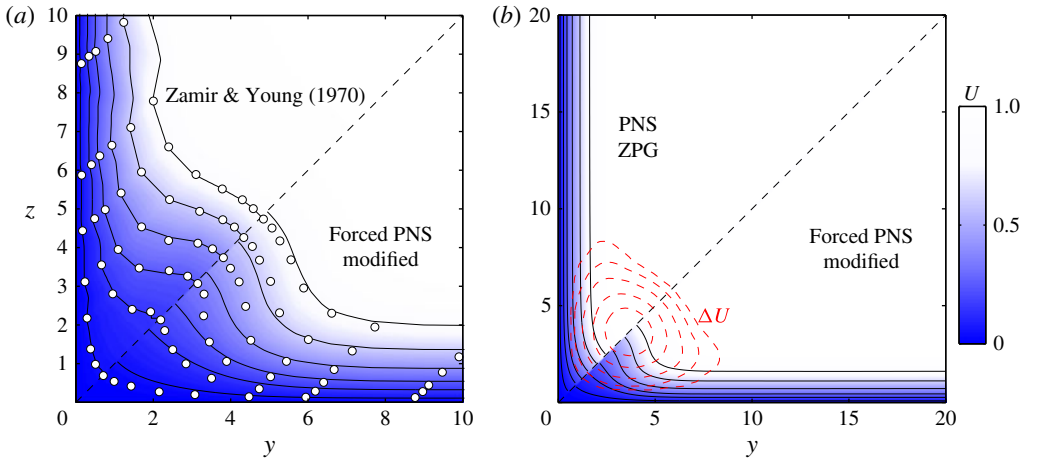

FIGURE 5. (Colour online) Streamwise base-flow velocity U: (a) comparison between the flow-field reconstruction from the measurement data (○) by Zamir & Young (1970, p. 320, figure 4c) (upper left) and the forced PNS solution (lower right); (b) comparison between the unforced PNS or classical self-similar ZPG case (upper left) and the forced or modified solution (lower right). The streamwise momentum forcing distribution ΔU is also indicated by contours (- - -). Solid contour lines (——) correspond to 5 %, 15 %, 25 %, 40 %, 60 % and 80 % of u_∞.

the global non-modal computations are presented in § 4.3. We specifically address the influence of the localization width, the Reynolds number and optimization time.

4.1. *Laminar base states*

Figure 5 shows a three-way comparison between measurements by Zamir & Young (1970), and the canonical ZPG with the modified numerical base-states calculated as described in § 3.1. The forcing distribution ΔU used in the source term of the PNS streamwise momentum equation is calculated as the difference between the measurement data as depicted in figure 5(a) and the classical self-similar solution in figure 5(b) (upper left). The two-dimensional flow field depicted in 5(a) (upper left) is reconstructed from the point-wise hot-wire data points using MATLAB's Delaunay-triangulation-based interpolation scheme for scattered data (MATLAB 2013). As the measurement data is not perfectly symmetric (compare figure 5a), the average with respect to the corner bisector is taken prior to the interpolation. It can be seen from the figure that the outward-bulge-shaped deformation is well approximated by our model, especially when considering the limited experimental source data. Also note that the exact form of the deformation is highly dependent on the leading-edge geometry and the local position along the plate. Here, we solely aim at reproducing this distinct feature in one possible realization for a qualitative comparison with the canonical solution.

The lower-wall-normal cross-flow velocity field is shown in figure 6 for the ZPG (6a) and the modified base state (6b). The streamlines illustrate how the displacement effect of the adjacent walls pushes fluid out of the computational domain along the bisector while fluid is sucked into the domain close to the walls. By comparing the cross-flow velocity distribution of the two cases, it can be seen that the flow field

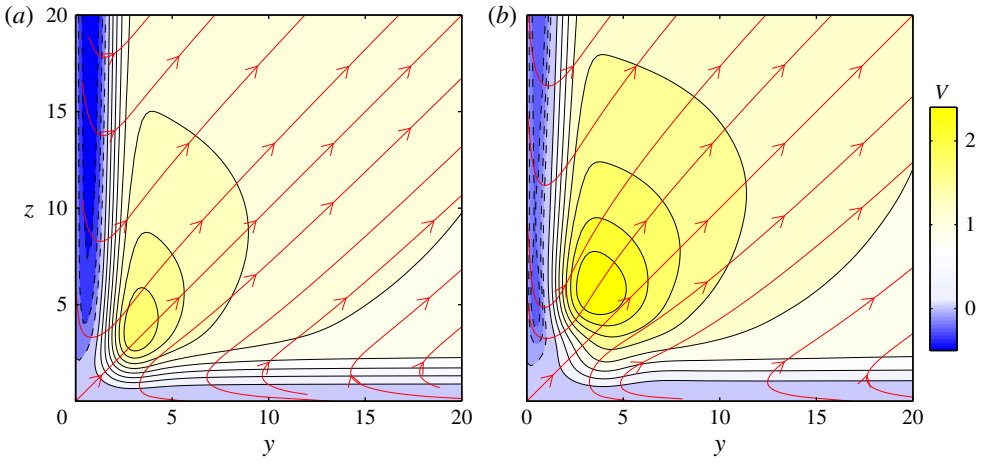

FIGURE 6. (Colour online) Isocontours of the base-flow velocity component normal to the lower wall V, and streamlines (red line) of the cross-flow velocity field (contours, black line $V > 0$, dashed line $V \leqslant 0$): (*a*) ZPG case; (*b*) modified case.

becomes distorted by the local forcing. However, the difference is subtle compared with the distinct qualitative deformation of the streamwise velocity field previously seen in figure 5(*b*). Note that the velocity fields shown in figures 5 and 6 depict only a part of the $y, z \in [0, 0] \times [50, 50]$ size domain for clarity. At the given domain size, both, the modified and the non-modified flow fields smoothly approach the asymptotic far-field solution without any distortion. For the local stability analyses in § 4.2 and the numerical simulations in § 4.3, the base states are truncated to $y, z \in [0, 0] \times [35, 35]$ and $y, z \in [0, 0] \times [45, 45]$, respectively.

4.2. *Local stability*

Finding eigensolutions to the combined Orr–Sommerfeld/Squire system (or the compressible counterpart) is the classical tool of local linear stability theory. In the following, the linear stability behaviour of the two base states is studied with a special focus on the effect of the base-state deformation. In the context of the global non-modal stability study to follow, the critical parameters obtained from local theory are crucial to determine where to expect exponential growth, and to choose the computational domains accordingly. The local linear stability and sensitivity of the two base states is considered in the following. In particular, the base-flow deformation is investigated in terms of its effect on modal shapes, neutral stability and eigenvalue sensitivity. Motivated by the inviscid instability mechanism present in corner flow, we further investigate the geometric features of the transversal base states in order to relate them to the Rayleigh–Fjørtoft necessary criterion.

4.2.1. *Modal shapes*

Owing to the basic symmetry of the base state, the solutions to the linear stability EVP (2.3) can be either even- (tagged E) or odd-symmetric (tagged O) with respect to the corner bisector. As we consider two-dimensional eigensolutions, the spanwise modulation of the viscous (Tollmien–Schlichting-type) modes along the walls is resolved. However, domain truncation renders the set of resolved spanwise

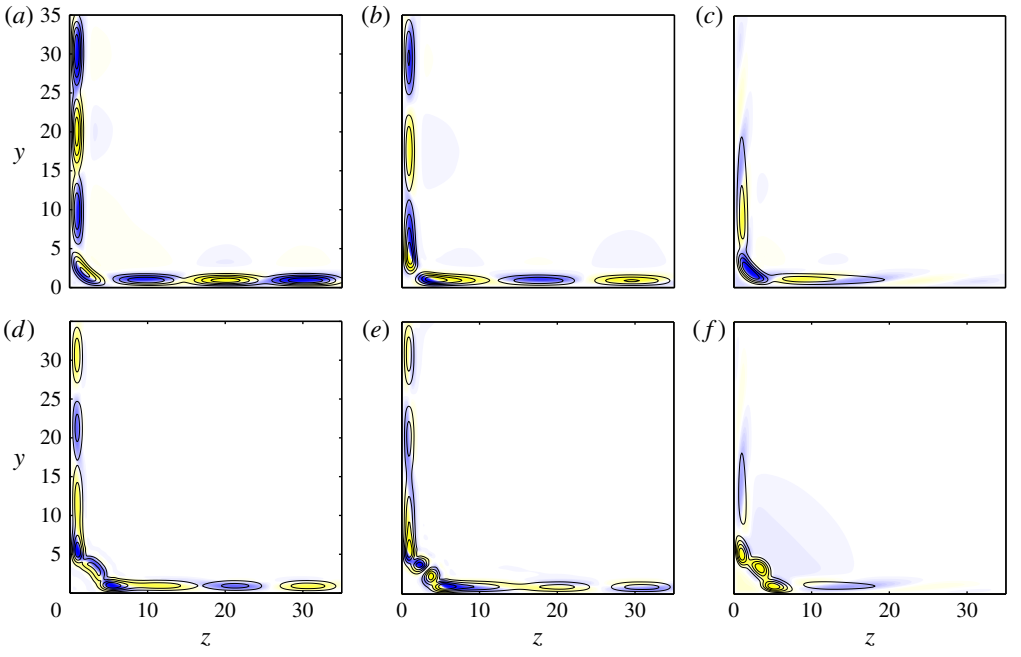

FIGURE 7. (Colour online) Selected modes for the ZPG solution (top row, *a–c*), and the modified solution (bottom row, *d–f*) for $Re_x = 4 \times 10^4$, $\omega = 0.1$: (*a,d*) IV-E; (*b,e*) IV-O; (*c,f*) corner mode *C*. The real part of the streamwise perturbation velocity is visualized by continuous contours (blue shade for $\mathrm{Re}(\hat{u}) > 0$, yellow shade for $\mathrm{Re}(\hat{u}) < 0$), and the streamwise perturbation velocity amplitude $|\hat{u}|$ by solid lines (——).

wavenumbers discrete, i.e. the spanwise domain extent enforces a fundamental wavelength and the viscous modes form a discrete branch of pairs of even- and odd-symmetric modes in the spectrum. The associated fundamental viscous mode is named I, the first harmonic II and so on. Apart from the viscous modes, the corner-flow problem features an inviscid mechanism represented by the corner mode *C*. Figure 7 shows the same three modes for the ZPG (*a–c*) and the modified base state (*d–f*), respectively, as examples. An even-/odd-symmetric pair of modes of the same spanwise wavenumber is shown in figure 7(*a,b* and *d,e*), respectively. For example, odd-symmetry becomes apparent when comparing the sign of the real part of the streamwise velocity perturbation in 7(*b,e*) along the adjacent walls. The reader is referred to the original article by Parker & Balachandar (1999) for a detailed discussions of modal shapes and amplification rates, and their dependence on the computational domain size, far-field boundary conditions as well as their relation to the two-dimensional Blasius boundary layer. From figure 7(*c,f*), it becomes evident that the corner mode has compact support in the near-corner region and is even-symmetric with respect to the bisector. By comparing the modal shapes for the two base states, one recognizes a distortion of the modes in the near-corner region that follows the bulge-shaped deformation of the modified base state. It can also be seen that the maximum perturbation amplitude is shifted towards the near-corner region for the latter base flow.

For one-dimensional velocity profiles, inviscid instability can be expected if the Rayleigh–Fjørtoft necessary criterion is met, i.e. if the position of the critical

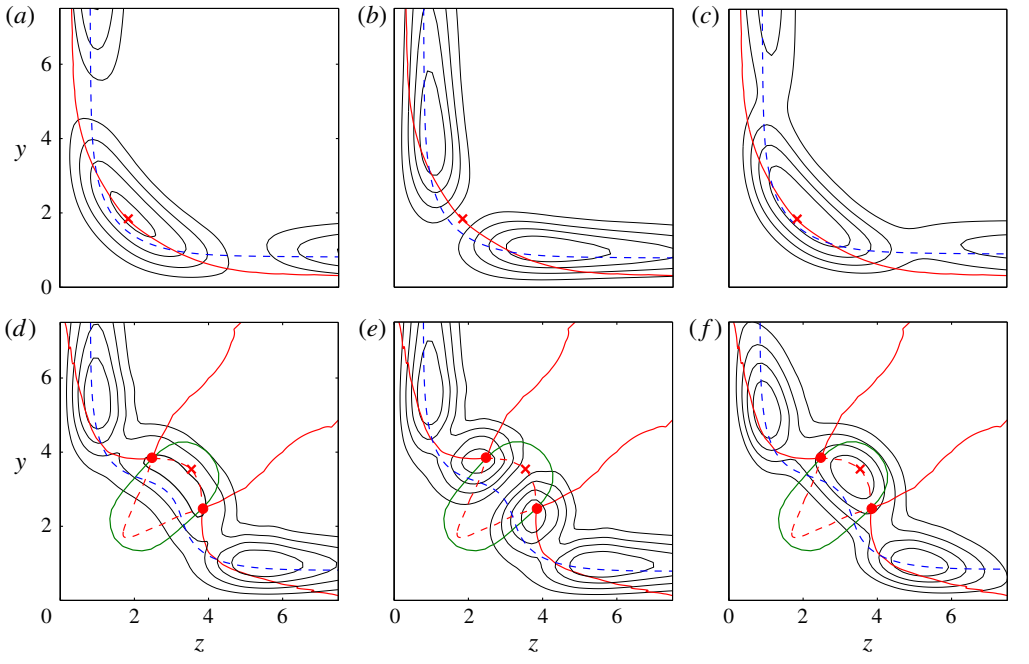

FIGURE 8. (Colour online) Geometric features of the ZPG (*a–c*) and the modified (*d–f*) base-state compared with the absolute value of $|\hat{u}|$ (black line) for selected modes: (*a,d*) IV-E; (*b,e*) IV-O; (*c,f*) corner mode. The principal curvatures k_1 (red line) and k_2 (dashed red line), the zero contour of the mean curvature (green line), flat umbilic points (●), $\partial^2 U(s)/\partial s^2 = 0$ (×) and the critical layer (dashed blue line) are visualized for comparison. The zero contour of the Gaussian curvature corresponds to (red line ∪ dashed red line). The same modes as in figure 7 are depicted.

layer coincides with an inflexion point of the base profile (see e.g. Drazin & Reid 2004). Early analyses of the streamwise corner-flow configuration were limited to the one-dimensional blending or bisector boundary layer due to the computational restrictions at the time, and the latter argument was used to establish the presence of an inviscid instability mechanism. No such general criterion exists for two- or three-dimensional flows, and it is not clear whether the analysis of a local profile is a valid approach. In figure 8, we compare some geometric features of the base states with the eigenmodes previously shown in figure 7. For surfaces in the three-dimensional Euclidean space, the concept of an inflexion point is ambiguous as more than one definition of curvature is conceivable. Commonly, the Gaussian curvature $K = k_1 k_2$, and the mean curvature $H = (k_1 + k_2)/2$ are defined through the principal curvatures k_1 and k_2, i.e. the maximum and minimum curvatures on the tangential surface at each point. The inflexion point of the one-dimensional bisector profile is given as a reference. It can be seen that the shape of the modes approximately follows the critical layer, as expected. Both base states are found to possess a zero line in the Gaussian curvature that coincides with the inflexion point along the bisector. The maximum velocity perturbation along the bisector is found in the vicinity of the inflexion point for all even-symmetric modes. A zero line in the mean curvature is only found for the modified base state, creating two flat umbilic points where $K = H = 0$. It is conspicuous that the maxima of the perturbation velocity

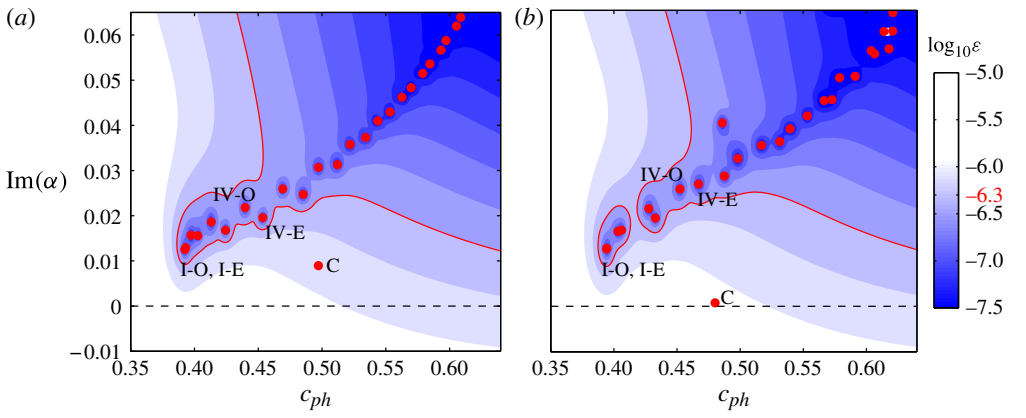

FIGURE 9. (Colour online) Eigenvalue spectrum (●), and ε-pseudospectrum (contours) for $Re_x = 4 \times 10^4$, $\omega = 0.1$: (*a*) self-similar solution; (*b*) modified solution. A particular value of $\varepsilon = 10^{-6.3}$ is highlighted by (——) for direct comparison, and the modes shown as examples in figures 7–9 are denoted by their names. Note that the eigenvalues of the leading odd- (I-O) and even-symmetric (I-E) viscous modes almost coincide. $c_{ph} = \mathrm{Re}(\omega)/\mathrm{Re}(\alpha)$ denotes the phase speed.

amplitude coincide with the latter points for the odd-symmetric mode depicted in figure 8(*e*). In fact, this is found to be the case for all odd-symmetric modes. Unfortunately, no criterion analogous to Rayleigh–Fjørtoft's necessary condition exists for higher dimensions. Therefore, interpretations in terms of a possible connection between the geometric features discussed above and hydrodynamic stability remain speculative. Here, we just note that the modified base state features a much richer set of geometric features in the near-corner region as compared with the ZPG case, potentially alternating the flow's global stability properties, as well.

4.2.2. *Eigenvalue spectrum and sensitivity*

Eigenvalue spectra for the modified and the ZPG base state obtained for the same representative parameter combination are compared in figure 9(*a,b*), respectively. In both cases, the viscous modes form an arc-shaped branch built of pairs of even- and odd-symmetric modes, while the corner mode appears isolated in the spectrum. By comparing the spectra, it can be seen that the viscous branch remains mostly unaffected from the modification. In contrast, the corner mode is shifted by a significant amount of $\Delta\mathrm{Im}(\alpha) \approx -0.01$ towards the unstable half-plane. The sensitivity of the linear operator in terms of the resolvent is addressed in the same figure. It is observed that the distribution of the resolvent is primarily linked to the course of the viscous branch. As a general trend, the areas of highest sensitivity (apart from in the vicinity of an eigenvalue where it becomes singular) are found in the region where the viscous branch approaches the continuous spectrum, i.e. towards the continuous branch at $c \approx 1$. This observation of highest sensitivity near branch junctions is commonly made in shear flows (see e.g. Schmid & Henningson 2001). The overall distribution of the resolvent is very similar between the two base states. This indicates that the base state modification does not significantly affect the sensitivity. In both cases, no deformation of the resolvent contours can be seen in the vicinity of the eigenvalue of mode *C*. The above observations are found in agreement with the sensitivity study

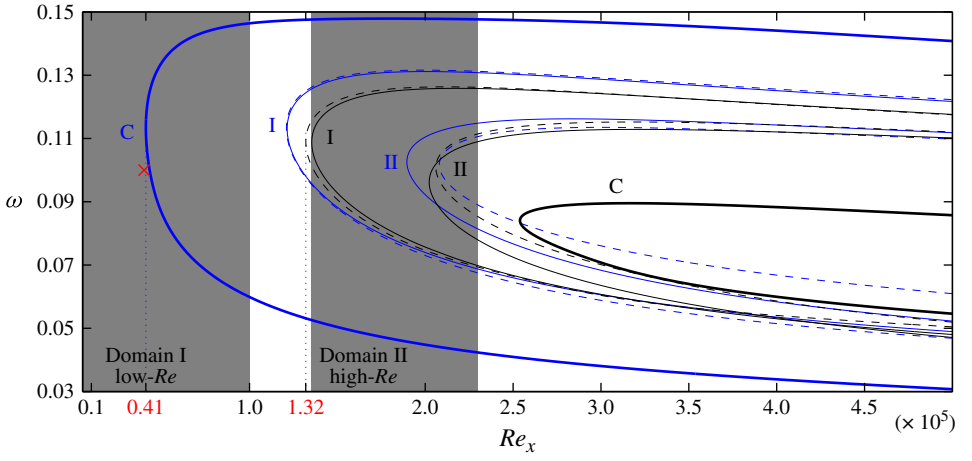

FIGURE 10. (Colour online) Neutral stability curves of the five leading modes of the ZPG (black shade), and the modified (blue shade) base flow. Solid lines (——) mark even-symmetric, dashed lines (- - - -) odd-symmetric and thick lines the corner mode. The critical parameters are $(Re_{x,c}, \omega_c) = (4.10 \times 10^4, 0.113)$ and $(Re_{x,c}, \omega_c) = (1.32 \times 10^5, 0.110)$ for the modified and the self-similar base state, respectively. The parameter combination $(Re_x, \omega) = (4 \times 10^4, 0.1)$ used in figures 7–9 is marked by (grey shade). The shaded areas (×) represent the low-*Re* and the high-*Re* computational domains investigated in §§ 4.3.2 and 4.3.3, respectively.

by Alizard *et al.* (2010). The authors used a minimal-defect-theory-based approach to calculate the sensitivity of the eigensolutions with respect to base-flow modifications in form of a so-called $\Delta \boldsymbol{U}$ pseudospectrum, analogous to the ε pseudospectrum. They demonstrated that small deviations of the base-state located in the near-corner region can drastically reduce the critical Reynolds number. In accordance with our results, they were able to associate the effect directly to the inviscid corner mode.

4.2.3. *Neutral stability*

Figure 10 shows neutral stability curves of the four leading viscous modes and the corner mode for both base flows. The neutral curves are obtained from the solution matrices outlined in table 1. Individual modes were tracked through cross-correlation of the eigenfunctions. It can be seen that the modified base state has a much lower critical Reynolds number of $\approx 0.41 \times 10^5$ as compared with the ZPG case with $\approx 1.32 \times 10^5$. Also note that the critical value occurs for the viscous mode I-O in the latter case, whereas the inviscid instability mode *C* is found critical for the modified case. A similar critical angular frequency of ≈ 0.11 is found for both cases. By comparing the neutral behaviour of the viscous and the inviscid modes between the two base states, it becomes evident that the modification mainly afflicts the inviscid mechanism represented by the corner mode. The less-significant effect on the Tollmien–Schlichting-type instabilities is explained by the fact that the viscous modes are related to the flat-plate boundary layers along the walls, whereas the corner mode is predominantly active in the near-corner region that is alternated by the modification. In the discussion of figure 9, the same observation was made for one representative choice of parameters. The result is also found in agreement with the observations previously made in the context of the base-state geometry, as shown in

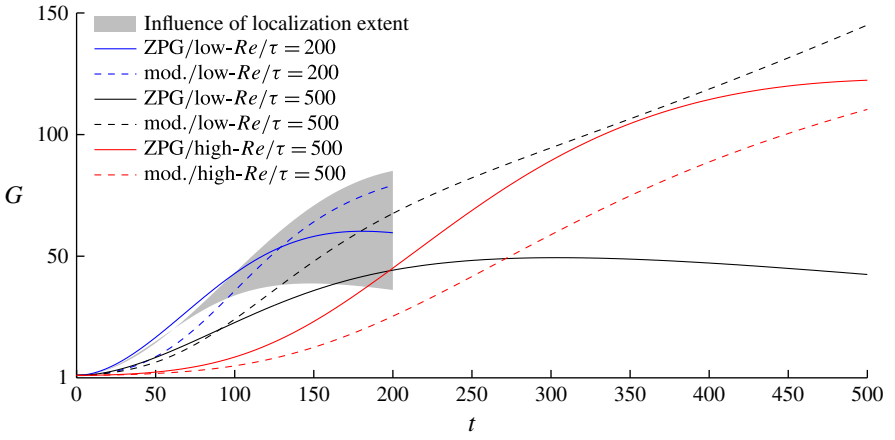

FIGURE 11. (Colour online) The transient energy growth factor G is plotted over time. Curves for the ZPG and modified base state are solid and dashed, respectively. Matching colours indicate the same Re–τ parameter combination. The grey area illustrates the difference between the short and a long streamwise localization extent, compare figure 3.

figure 8. The neutral stability behaviour seen from figure 10 motivates our choice of computational domains (compare table 2): the high-Re domain is supercritical for the leading viscous modes, while the low-Re domain is subcritical for the viscous modes, and partly supercritical for the corner mode for the modified base state only. Note that the critical Reynolds number of $\approx 0.41 \times 10^5$ is close to the value of $\approx 0.6 \times 10^5$ as found by Parker & Balachandar (1999) in their study of the classical self-similar corner-flow solution with an adverse pressure gradient. However, the results cannot be compared directly as our approach mimics a localized pressure gradient, whereas the above authors assumed a Falkner–Skan-type potential pressure variation along with the consequential dependence of the freestream velocity on the streamwise position. The solutions to the resulting non-ZPG corner-layer equations do not possess the experimentally observed local deformation as mimicked by the modified base state.

4.3. *Optimal perturbations*

Optimal perturbations are calculated using the procedure outlined in § 3.3 for six combinations of the parameters base state (ZPG or modified) Reynolds-number regime (low-Re or high-Re, see figure 10) and optimization time ($\tau = 200$ or $\tau = 500$). Two additional calculations are conducted for the sole purpose of determining the influence of the optimal initial condition localization area Λ. Figure 11 gives an overview of the calculations performed in terms of the global transient growth factor G as defined in (2.5). In any case, spatial transient growth with potential energy gains between one and two orders of magnitude is observed. A comparative study of the effect of the artificial spatial localization is conducted in the following § 4.3.1.

4.3.1. *Influence of the streamwise localization width*

The spatial confinement of the optimal initial perturbation to a subset $\Lambda \subset \mathscr{D}$ as described in § 3.3 certainly restricts the generality of our results. Therefore, the effect of the spatial restriction is studied in order to ensure that its influence does not interfere with physical indications of interest. The optimal initial conditions are

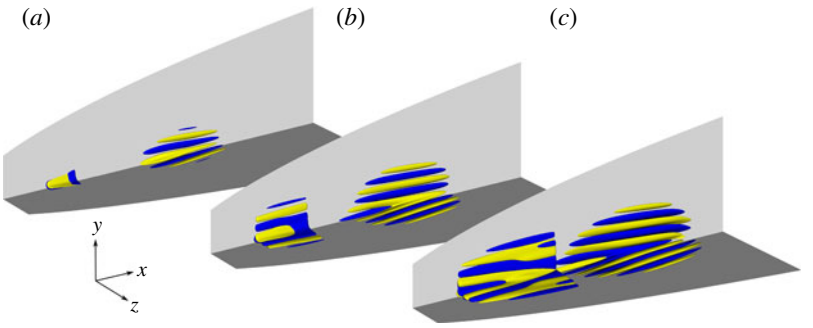

FIGURE 12. (Colour online) Influence of the streamwise localization width on the optimal initial condition (upstream wavepackets) and response (downstream wavepackets) for the ZPG/low-$Re/\tau = 200$ case: (*a*) short; (*b*) intermediate; (*c*) long streamwise localization extent. The corresponding windowing functions are shown in figure 3. The initial condition and response are shown in the same plot for comparison. Isosurfaces of the streamwise perturbation velocity (blue shade for $u' > 0$, yellow shade for $u' < 0$) are depicted.

Re	Low	Low	Low	Low	High
τ	200	200	200	500	500
σ_A	Short	Medium	Long	Medium	Medium
$G(\tau)$	36.1	59.7 {79.16}	85.1	42.5 {145.0}	122.3 {110.3}
G_{max}	38.8	60.2 {79.16}	85.1	49.4 {145.0}	122.3 {110.3}
$t(G_{max})$	148	181 {200}	200	303 {500}	500 {500}

TABLE 3. Values of the transient energy gain at $t = \tau$, maximum energy gain, and time at which the maximum gain occurs: ZPG base state and {modified base state}.

artificially localized in the streamwise direction only. In addition, the spanwise restriction due to the finite computational domain extent has to be addressed. Figure 12 shows the optimal initial perturbations and responses for the ZPG/low-$Re/\tau = 200$ case for the three different windowing functions corresponding to the short, intermediate and long streamwise localization extents. It can be seen that the initial conditions and responses take the form of wavepackets that are confined in both, the streamwise and the spanwise directions. The effect of the artificial windowing in the streamwise direction of the initial perturbations can clearly be seen. In contrast, the confinement of the structures in the spanwise directions, i.e. to the near-corner region, is a result of the optimization process. In all three cases, the optimal response appears in form of an elongated perturbation pattern or streaks, that are slightly tilted towards the corner. All structures are found to be symmetric with respect to the corner bisector. With increasing localization width, the optimal response is found to grow in space without changing its basic characteristics in terms of orientation or wavenumber in any direction. Similarly, the transient energy growth factor G as shown in figure 11 (grey area and blue line) increases with increasing localization width. This cannot be explained by the mere growth of the response wavepacket as the growth factor directly relates the integral energy norms of the response to the initial condition. The values of the maximum and final energy gain for all eight parameter combinations are summarized in table 3.

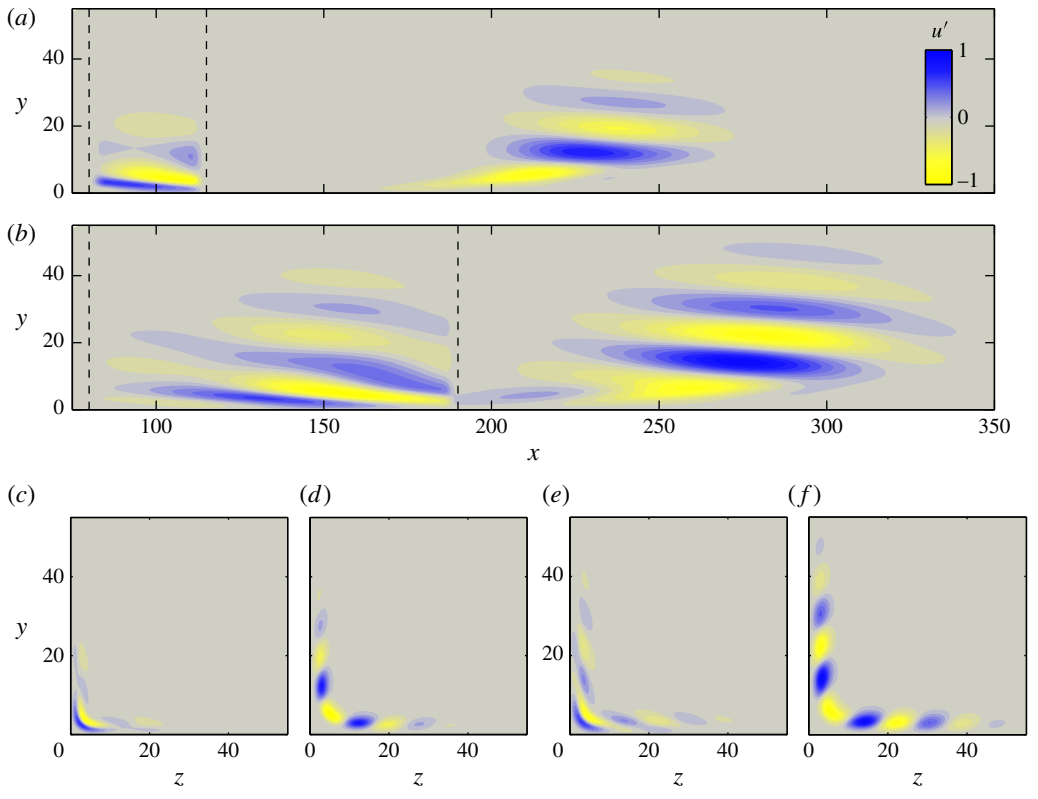

FIGURE 13. (Colour online) Streamwise perturbation velocity u' for the low-Re regime and $\tau = 200$ upon the ZPG base state: (a) short and (b) long localization width case in the x–y-plane at $z = 1.5\delta^*$ (optimal initial condition and response are depicted in the same plot as in figure 12, and the localization width is indicated by dashed lines); optimal initial condition for the (c) short and (e) long case and optimal response for the (d) short and (f) long case in the transversal plane at $x = \arg\max_x \boldsymbol{u}'$.

The short and long localization width cases are compared in more detail in figure 13. By comparing the optimal initial conditions between the cases in figure 13(a,b), respectively, it can be seen that the maximum of the perturbation velocity for the long case is found at $x \approx 130$, i.e. downstream of the confinement region of the short case. Since the short confinement region is a subset of the long one, the optimal energy gain, in fact, has to be higher in the latter case. A closer look at the initial conditions in 13(c,e) and responses in 13(d,f) shows that both structures are similar between the cases despite a somewhat increased spanwise extension in the long case. In the following, the intermediate windowing function is used for all calculations and we expect no qualitative effect on the optimal solutions caused by the exact streamwise extent of the windowing for the above reasoning.

4.3.2. *Subcritical-Reynolds-number regime (low-Re)*

In the subcritical-Reynolds-number regime, non-modal growth is of special interest as it potentially leads to a bypass of the classical transition scenario caused by Tollmien–Schlichting waves. As demonstrated by Schmidt & Rist (2014), non-modal growth plays an important role in streamwise corner flows as it occurs naturally,

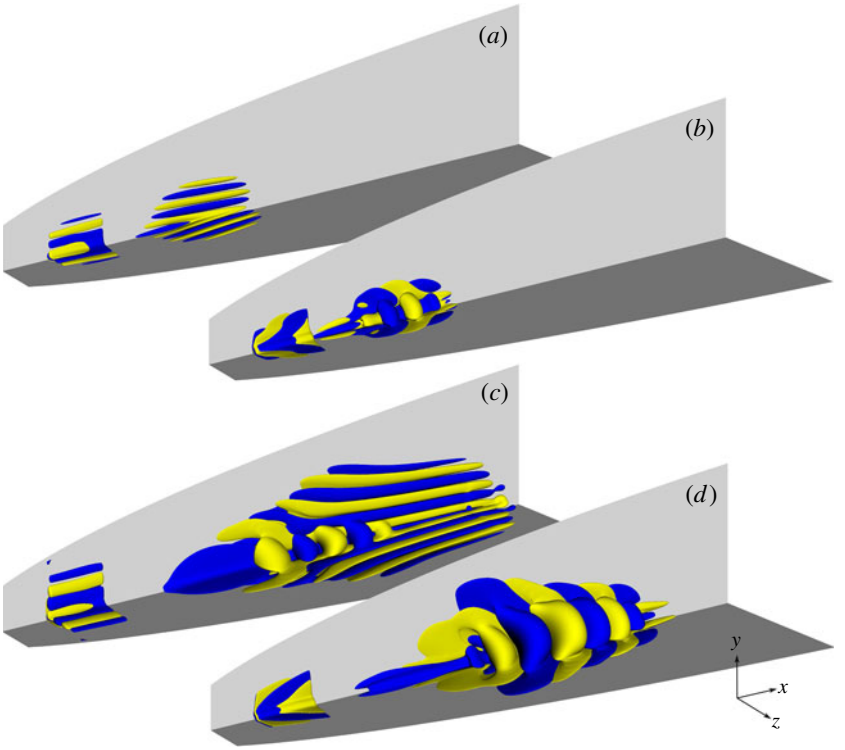

FIGURE 14. (Colour online) Same as figure 12 for the low-*Re* cases: (*a*) ZPG base state with $\tau = 200$; (*b*) modified base state with $\tau = 200$; (*c*) ZPG base state with $\tau = 500$; (*d*) modified base state with $\tau = 500$.

even if the flow is harmonically forced. The underlying mechanism was traced back to a resonance between the inviscid corner mode and viscous Tollmien–Schlichting modes. Here, we examine the non-modal worst-case scenario in particular, and place a special focus on the effect of the base-flow modification.

Figure 14 gives an overview of the four calculations conducted in the low-*Re* regime. As would be expected, the optimal response for the long optimization time of $\tau = 500$ (*c*,*d*) is more widespread as compared to the $\tau = 200$ (*a*,*b*) calculations in both the streamwise and the spanwise directions. Most importantly, however, the structure of the response wavepackets qualitatively differs between the ZPG (14*a*,*c*) and the modified (14*b*,*d*) base state cases. In the latter case, the response appears modulated in the streamwise direction while the previously described streaks are unmistakable for the ZPG base state. Quantitative implications of the two different response variants in terms of the transient energy gain can be deduced from figure 11. For both optimization times (blue lines for $\tau = 200$, black lines for $\tau = 500$), the maximum transient energy level is attained at $t = \tau$ for the modified base states (dashed lines). The ZPG base-state calculations reach their maximum value of G for some $t < \tau$, i.e. at $t \approx 180$ and $t \approx 300$ for $\tau = 200$ and $\tau = 500$, respectively. All curves exhibit a significant initial energy gain that can be traced back to the non-modal growth mechanisms, as explained later in more detail. After the initial phase, modal growth in accordance with the neutral stability estimates shown in figure 10 dominates. This can be seen particularly well for the $\tau = 500$ cases. The

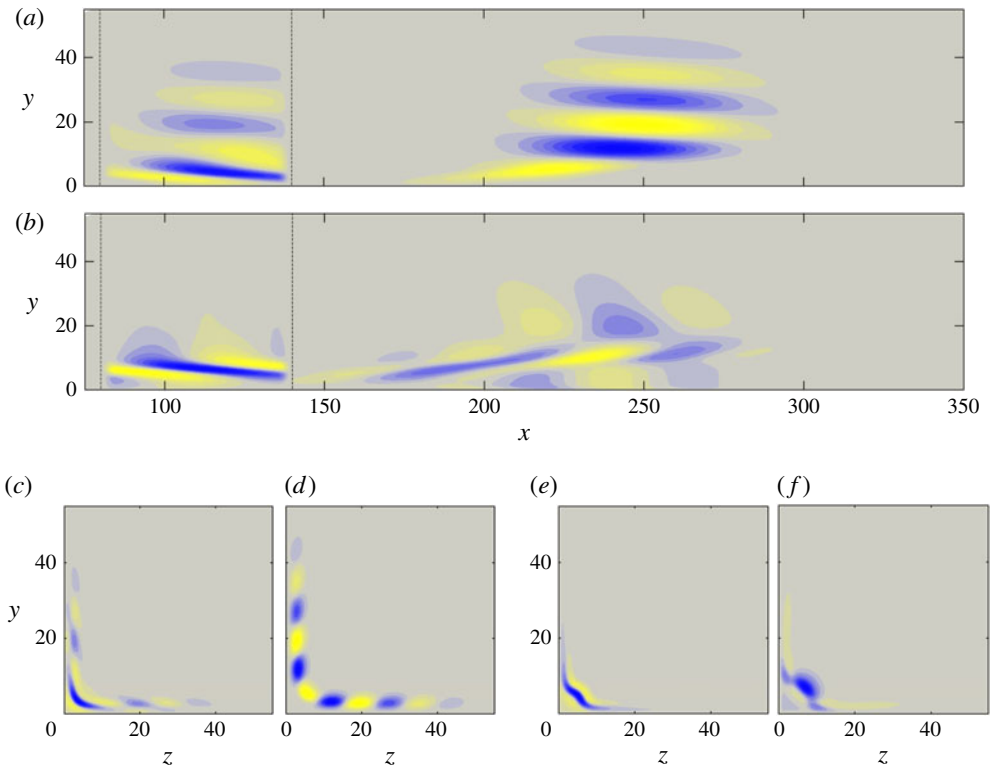

FIGURE 15. (Colour online) Streamwise perturbation velocity u' of the optimal initial condition and response for the low-Re regime and $\tau = 200$: (a,c,d) ZPG; (b,e,f) modified (same planes as in figure 13).

ZPG simulation exhibits exponential decay, whereas the modified base state supports an instability in form of the corner mode for $Re_{x,c} \geqslant 4.1 \times 10^4$. Both effects are clearly observed after the initial transient amplification phase.

The optimal initial conditions and responses for $\tau = 200$, and $\tau = 500$ are further detailed in figures 15 and 16, respectively. By comparing the two, we note that the difference in optimization time does not alter the general structure of neither the optimal initial condition, nor the corresponding response. The spatial structure of the initial condition in the region close to the opposing wall at $y \lesssim 10$ is very similar in all four cases, whereas precursors of the later streaks can be seen for the ZPG cases in figures 15(a) and 16(a) that are not present for the modified flow in figures 15(b) and 16(b). The optimal responses for the modified flow as depicted in figures 15(f) and 16(f) show a certain resemblance to the corner-mode as seen in figure 7(f). For the $\tau = 500$ case, this observation is expected from classical linear theory as noted above, and further confirmed by the exponential energy growth observed from figure 11.

The cause of the transient energy growth is further investigated by examining the optimal structures in the bisector plane in figure 17. The typical footprint of the Orr mechanism can be seen for both, the ZPG and the modified case, in figure 17(a,b), respectively: the optimal initial structure is modulated and leans against the mean shear, while the optimal response is aligned with the mean shear. Therefore, the Orr

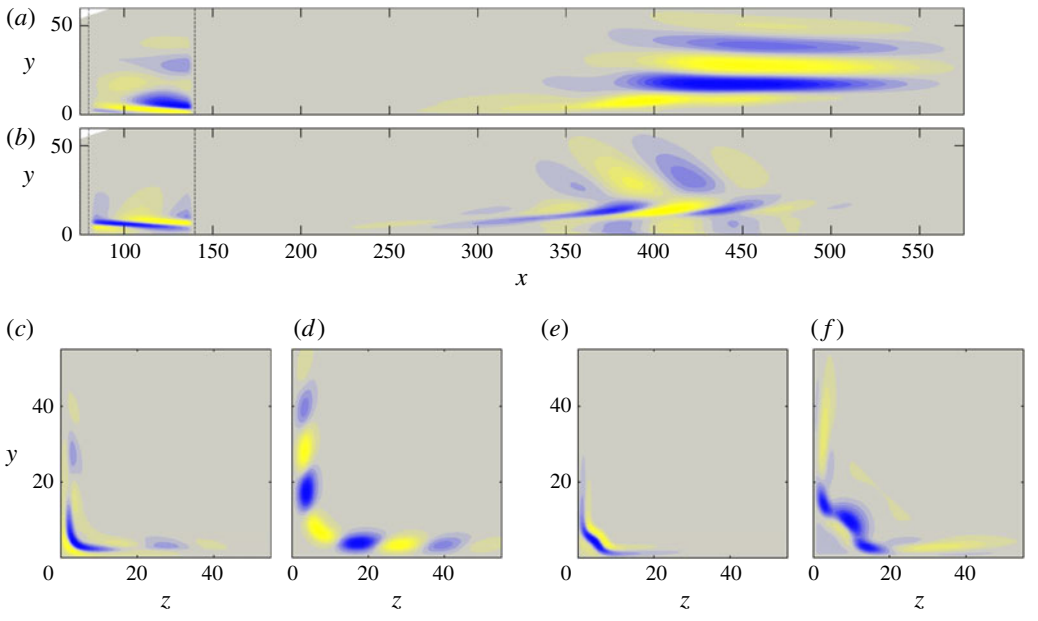

FIGURE 16. (Colour online) Streamwise perturbation velocity $\boldsymbol{u}'$ of the optimal initial condition and response for the low-Re regime and $\tau = 500$: (a,c,d) ZPG; (b,e,f) modified (same planes as in figure 13).

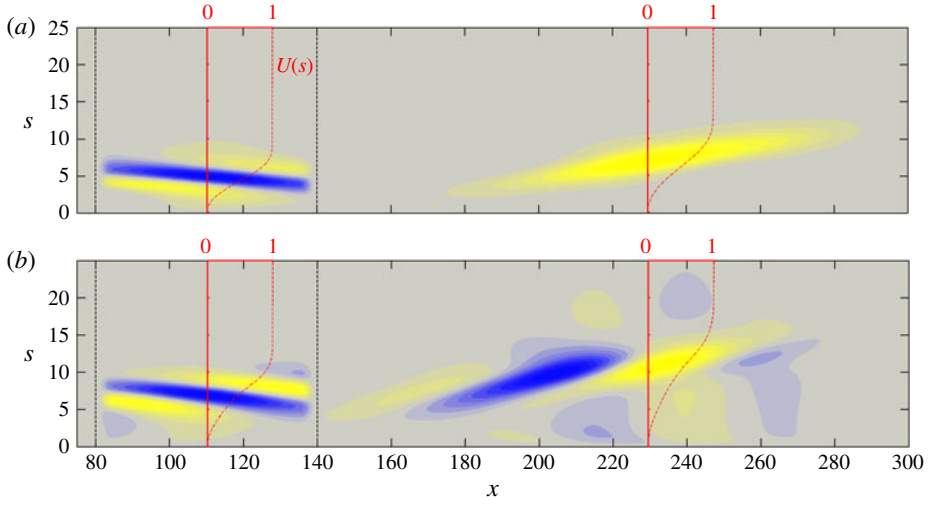

FIGURE 17. (Colour online) Streamwise perturbation velocity u' of the optimal initial condition and response for the low-Re regime and $\tau = 200$ in the bisector-plane: (a) ZPG and (b) modified base state. Profiles of the streamwise base-flow velocity U are shown for comparison (red axes).

mechanism is identified as the origin of the initial energy growth observed in figure 11, i.e. at least for the modified cases where the optimal response manifests in form of a streamwise modulated wavepacket.

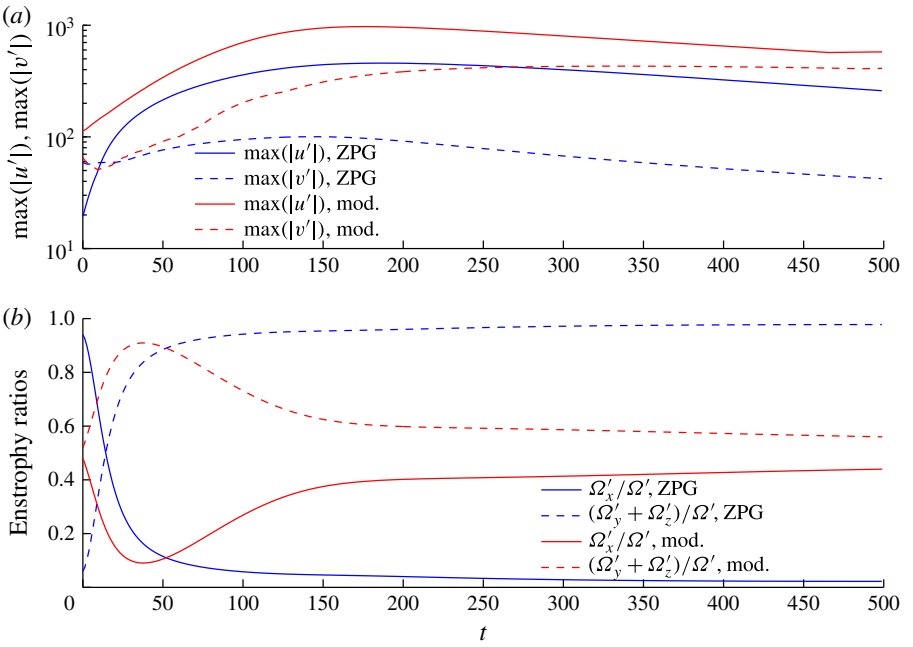

FIGURE 18. (Colour online) Temporal evolution of the optimal initial solution of both base states for the low-*Re* regime and $\tau = 500$: (*a*) maximum absolute value of the streamwise, u', and crossflow, v', velocity (note that $\max(|w'|) = \max(|v'|)$); (*b*) normalized streamwise and transverse perturbation enstrophy components (again, $\Omega'_y = \Omega'_z$ owing to symmetry).

For the ZPG base states, the streaky structure of the optimal response suggests the presence of the lift-up mechanism. The latter conjecture is confirmed by considering the component-wise perturbation velocity evolution of the optimal as shown in figure 18(*a*). During the initial stage at $t \lesssim 10$, the crossflow component is dominant for the ZPG (blue lines) base state but is rapidly overtaken by the strongly amplified streamwise component. The underlying evolution of streamwise streaks from vortical structures in the transverse plane is characteristic of the lift-up mechanism, and was similarly observed by Monokrousos *et al.* (2010) for the flat-plate boundary layer. Alternatively, the perturbation enstrophy and its directional components defined as

$$\Omega' = \int \boldsymbol{\omega}' \cdot \boldsymbol{\omega}' \mathrm{d}\mathscr{D} \quad \text{and} \quad \Omega'_i = \int \omega_i'^2 \mathrm{d}\mathscr{D} \quad \text{for } i = x, y, z, \tag{4.1a,b}$$

respectively, can be investigated. Here, $\boldsymbol{\omega}' = [\omega'_x\ \omega'_y\ \omega'_z]^{\mathrm{T}} = \boldsymbol{\nabla} \times \boldsymbol{u}'$ is the perturbation vorticity vector. In the present context, the enstrophy serves as a bulk measure of the vorticity. The temporal evolutions of the normalized perturbation enstrophy ratios of the ZPG (blue lines) and modified (red lines) are compared in 18(*b*). It can be seen that the initial solution for the ZPG base state at $t = 0$ predominantly consists of streamwise vorticity. During the initial stage of transient amplification, vorticity is transferred from the streamwise to the transverse components until the roles have almost completely reversed for $t \gtrsim 100$. The exact same behaviour was found by Alizard *et al.* (2012) in their parallel setup for a fixed streamwise wavenumber of $\alpha = 0$, and again attested to the lift-up mechanism. In contrast, the sum of the

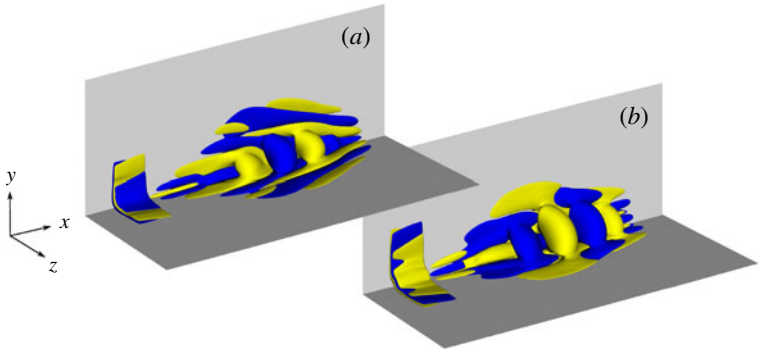

FIGURE 19. (Colour online) Same as figure 12 for the high-*Re* cases: (*a*) ZPG base state with $\tau = 500$; (*b*) modified base state with $\tau = 500$.

transverse components approximately matches the streamwise component at $t = 0$ in the modified (red lines) case. Subsequently, the perturbation undergoes a transient process similar to the one observed for the ZPG base state, but finally returns to a more balanced distribution for $t \gtrsim 150$. The latter observation is consistent with the optimal response depicted in figure 16(*b*) which appears modulated in both the streamwise and spanwise directions.

4.3.3. *Supercritical-Reynolds-number regime (high-Re)*

In the supercritical regime, transient effects are expected to coexist with exponential growth (and will eventually be dominated by the latter for larger times). The three-dimensional and planar visualizations of the optimals in figures 19 and 20, respectively, dominantly show the signature of the streamwise modulated wavepacket associated with the Orr effect and/or modal growth prior to this. However, indications of streaks are also observed, especially in the near-corner region in 19(*a,b*). Seemingly, the optimal perturbation is still in its initial stage for the given computational domain length and optimization time (note that the dimensional time and confinement width are the same as in the low-*Re* simulations). This can more clearly be seen from the transient energy gain for the high-*Re* cases when compared with the low-*Re* base-state simulations in figure 11, and explains why the maximum gain is higher for the ZPG case. In the further development of the optimal or for longer optimization times, it is certainly expected that the modified base state will experience a higher maximum gain through exponential growth. The combined Orr and lift-up scenario is also apparent in the low-*Re* structures in figure 14(*b–d*), although somewhat less pronounced.

4.3.4. *Characteristic scales*

An overview of the characteristic streamwise and transverse length scales of the optimal initial conditions and responses is reported in table 4 in terms of the corresponding wavenumbers. For that purpose, the dominant wavelengths were manually measured from the one-dimensional streamwise perturbation velocity profiles in the streamwise and transverse directions as shown in figure 21(*a,b*), respectively. Alizard *et al.* (2012) reported a wavelength corresponding to a transverse wavenumber of $\beta_0 = 0.52$ for the symmetric optimal solution at a fixed Reynolds number of $Re_x = 0.8 \times 10^5$, and a fixed streamwise wavenumber of $\alpha = 0$. The corresponding

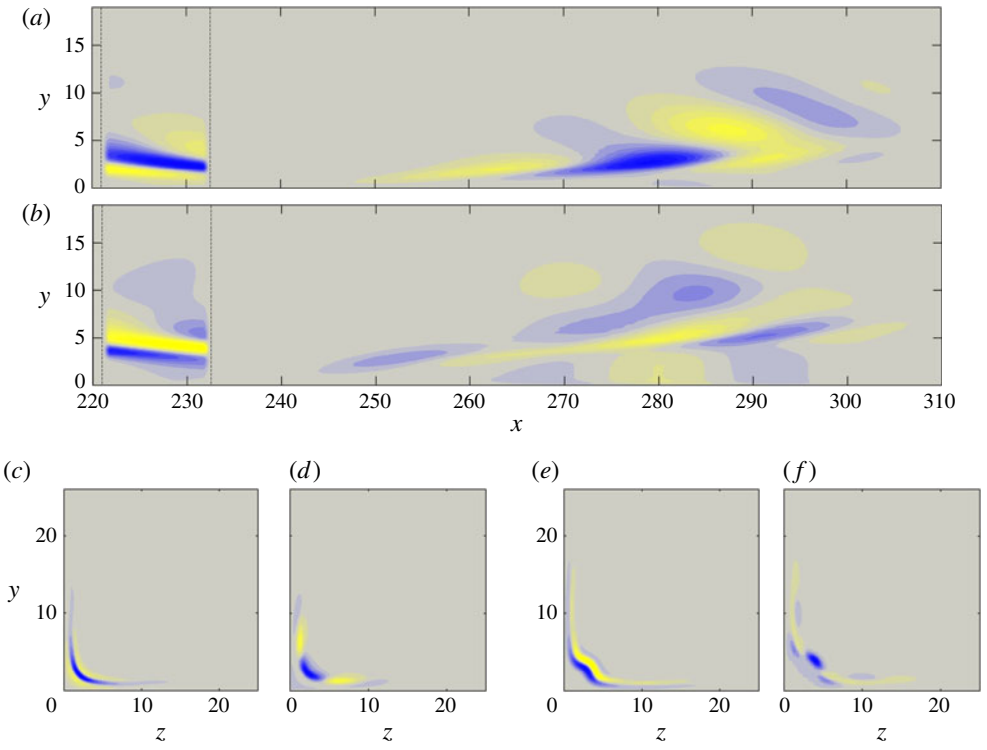

FIGURE 20. (Colour online) Streamwise perturbation velocity u' of the optimal initial condition and response for the high-Re regime and $\tau = 500$: (a,c,d) ZPG; (b,e,f) modified (same planes as in figure 13).

Re	Low	Low	Low	High
τ	200	200	500	500
σ_Λ	Long	Medium	Medium	Medium
α_0	$\approx\alpha_\Lambda$	$<\alpha_\Lambda$ $\{<\alpha_\Lambda\}$	$\approx\alpha_\Lambda$ $\{<\alpha_\Lambda\}$	$<\alpha_\Lambda$ $\{<\alpha_\Lambda\}$
β_0	0.63	0.63 $\{1.73\}$	0.47 $\{1.74\}$	– $\{-\}$
α_τ	≈ 0	≈ 0 $\{0.12\}$	≈ 0 $\{0.1\}$	0.27 $\{0.29\}$
β_τ	0.96	0.97 $\{-\}$	0.90 $\{-\}$	– $\{-\}$

TABLE 4. Characteristic scales of the optimal initial condition and responses: ZPG base state and {modified base state}. Here α and β denote the dominant streamwise and transverse wavenumbers, and subscript 0 and τ the optimal initial and response solution, respectively, α_0 is given in relation to the wavenumber corresponding to the localization width, i.e. $\alpha_\Lambda = 0.10$ and $\alpha_\Lambda = 0.057$ for the medium and long windowing function, respectively (compare figure 3) and '$-$' denotes a case where a dominant wavenumber was not clearly identifiable. Transverse wavenumbers β are normalized by the local displacement thickness for comparability.

value for the Blasius boundary layer is $\beta_0 = 0.54$. Similarly, we observe a value of $\beta_0 = 0.47$ in the subcritical low-Re regime, and a slightly inclined streaky response pattern with $\alpha_\tau \approx 0$.

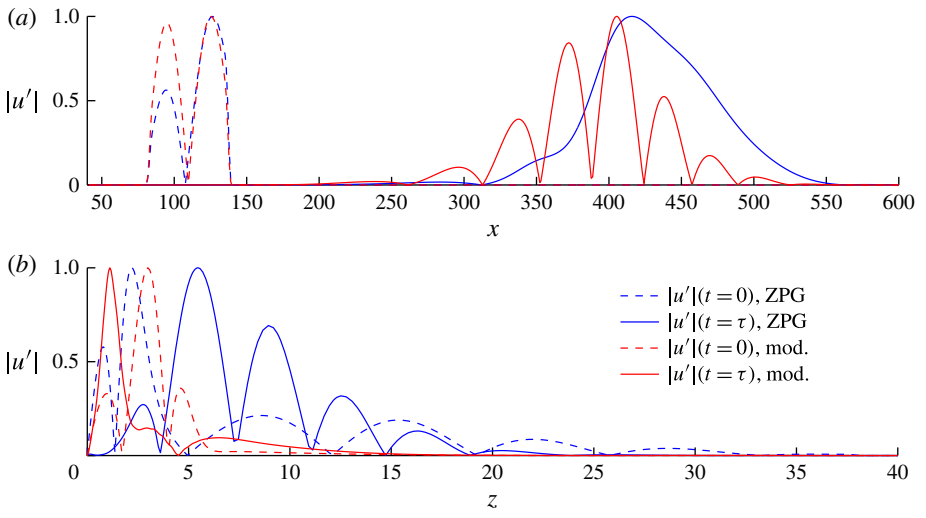

FIGURE 21. (Colour online) Profiles of the absolute value of the normalized streamwise perturbation velocity $|u'|$ for the low-Re case and $\tau = 500$: (a) along the streamwise coordinate; (b) in the spanwise direction. Profiles are plotted along the respective axis at the location of the global maximum within the domain. The normalization is with respect to the maximum value in $\mathscr{D}$.

5. Summary and conclusions

Streamwise corner flow is known to facilitate non-modal instabilities at low Reynolds numbers in the near-corner region (Schmidt & Rist 2014). The present study elaborates on the maximum possible transient growth of spatially restricted wavepackets calculated within an adjoint-based linear framework. Two base states are considered: the canonical self-similar corner-flow solution, and a second modified solution that mimics a characteristic deviation from the first mentioned ZPG case caused by leading-edge effects. Both base flows are obtained by solving the PNS. Prior to the global non-modal analysis, a classical local linear stability and eigenvalue sensitivity study is conducted. As a first important result, it is observed that the mean flow deformation hardly changes the local non-modal properties in terms of the ϵ pseudospectrum, but significantly reduces the critical Reynolds number. This result is in good agreement with the study by Alizard *et al.* (2010) who demonstrate that the self-similar corner-flow solution is highly sensitive with respect to modifications of the mean flow in the near-corner region, and offers a plausible explanation for the low transition Reynolds number found in experimental studies. In their study as well in the present work, the inviscid corner mode is associated with the instability. The geometry of the laminar base states is analysed to shed some light on the much lower inviscid instability limit of the modified flow. It is demonstrated that the modification further aggravates the inflectional nature of the base state.

Based on the findings of the linear stability analysis, a low- and a high-Reynolds-number regime domain are defined for the calculation of optimal wavepackets. Subsequently, spatially localized optimal initial perturbation and corresponding responses are obtained through direct-adjoint looping. The influence of the localization width, the optimization time, and the Reynolds number on the spatial structure of the optimals, and their transient energy amplification are studied in detail. For all

parameter combinations, optimal structures that cause significant transient energy gain are found. Geometrically, all optimals are compact in the sense that they are restricted to the corner region, and symmetric with respect to the corner bisector. In the low-Re case, the Orr and the lift-up mechanism are clearly identified as dominant sources of transient growth for the ZPG and the modified base state, respectively. In the case of harmonic forcing, suboptimal transient growth leading to moderate amplification factors of $G \lesssim 4$ was observed by Schmidt & Rist (2014). In comparison, the present global optimal solution for $\tau = 200$ and the ZPG base state attains a maximum growth of $G \approx 50$ in the subcritical-Reynolds-number regime.

Our results are also found in some contradiction to previous work by Alizard *et al.* (2012), who investigated the non-modal growth of the ZPG corner-flow solution within a parallel, i.e. temporal, framework for fixed streamwise wavenumbers. The authors found that maximum gain is obtained by antisymmetric optimal structures, whereas the power iteration-based method used in the present study consistently converged towards symmetric optimal solutions. The dominance of symmetric arrangements is supported by the DNS of Schmidt & Rist (2014). In the latter, the fully three-dimensional flow was forced harmonically by localized wall heating, and no transient energy amplification was detected downstream of the source in the case of asymmetric forcing. Symmetric forcing, however, leads to spatial transient growth caused by a non-modal interaction between the corner mode and the symmetric Tollmien–Schlichting mode branch. The different results are explained by the different paths taken to overcome the difficulties of the fully non-homogeneous set-up, i.e. the parallel flow assumption in the case of Alizard *et al.* (2012), and the artificial localization and restriction to certain optimization times in the present study. A truly global non-modal stability study as conducted by Sipp & Marquet (2013) for the two-dimensional flat plate flow would be desirable to further address non-parallel effects. Another key aspect to be considered in future studies is the role of nonlinearity as linear optimal perturbations do not necessarily provide the most efficient path to transition. In the closely related case of the flow in a square duct, Biau, Soueid & Bottaro (2008) found that the key mechanism for rapid transition is the generation of an unstable mean flow distortion that supports further exponential or algebraic growth. Along a similar train of thought, it was recently shown by Karp & Cohen (2014) that non-modal growth can lead to rapid transition in Couette flow through nonlinear interactions. The authors demonstrated that the key factor to cause a rapid breakdown is the ability of the transient growth process to induce inflexion points in the base state. The present results for the modified base state underline the potential of such a scenario. Therefore, a logical extension of the current work is to consider nonlinear optimal perturbations as in the work of Cherubini *et al.* (2010) or Monokrousos *et al.* (2011). DNS of a full finite plate-width corner set-up aimed at studying deviations from the self-similar base state and leading-edge receptivity are work in progress and show great promise.

Acknowledgement

O.T.S. acknowledges support from the Deutsche Forschungsgemeinschaft (DFG) under Grant No. RI 680/22. A.H. acknowledges support from the Swedish Research Council. Supercomputing time provided by the Swedish National Infrastructure for Computing (SNIC) and the Federal High-Performance Computing Center Stuttgart (HLRS) under project LAMTUR is gratefully acknowledged.

REFERENCES

ALIZARD, F., RIST, U. & ROBINET, J.-C. 2009 Linear instability of streamwise corner flow. *Adv. Turbulence* **12**, 67–70.

ALIZARD, F., ROBINET, J.-C. & GUIHO, F. 2012 Transient growth in a right-angled streamwise corner. *Eur. J. Mech. (B/Fluids)* **37**, 99–111.

ALIZARD, F., ROBINET, J.-C. & RIST, U. 2010 Sensitivity analysis of a streamwise corner flow. *Phys. Fluids* **22** (1), 014103.

ANDERSSON, P., BERGGREN, M. & HENNINGSON, D. S. 1999 Optimal disturbances and bypass transition in boundary layers. *Phys. Fluids* **11**, 134.

BAGHERI, S., BRANDT, L. & HENNINGSON, D. S. 2009 Input–output analysis, model reduction and control of the flat-plate boundary layer. *J. Fluid Mech.* **620**, 263–298.

BALACHANDAR, S. & MALIK, M. R. 1995 Inviscid instability of streamwise corner flow. *J. Fluid Mech.* **282**, 187–201.

BARCLAY, W. H. & RIDHA, A. H. 1980 Flow in streamwise corners of arbitrary angle. *AIAA J.* **18**, 1413–1420.

BIAU, D., SOUEID, H. & BOTTARO, A. 2008 Transition to turbulence in duct flow. *J. Fluid Mech.* **596**, 133–142.

BUTLER, K. M. & FARRELL, B. F. 1992 Three-dimensional optimal perturbations in viscous shear flow. *Phys. Fluids* A **4**, 1637.

CHERUBINI, S., DE PALMA, P., ROBINET, J.-C. & BOTTARO, A. 2010 Rapid path to transition via nonlinear localized optimal perturbations in a boundary-layer flow. *Phys. Rev.* E **82** (6), 066302.

CORBETT, P. & BOTTARO, A. 2000 Optimal perturbations for boundary layers subject to stream-wise pressure gradient. *Phys. Fluids* **12**, 120.

DHANAK, M. R. 1992 Instability of flow in a streamwise corner. NASA Contractor Rep. 191410, ICASE Rep. No. 92-70.

DHANAK, M. R. 1993 On the instability of flow in a streamwise corner. *Proc. R. Soc. Lond.* A **441**, 201–210.

DHANAK, M. R. & DUCK, P. W. 1997 The effects of freestream pressure gradient on a corner boundary layer. *Proc. R. Soc. Lond.* A **453** (1964), 1793–1815.

DRAZIN, P. G. & REID, W. H. 2004 *Hydrodynamic Stability*. Cambridge University Press.

EDWARDS, W. S., TUCKERMAN, L. S., FRIESNER, R. A. & SORENSEN, D. C. 1994 Krylov methods for the incompressible Navier–Stokes equations. *J. Comput. Phys.* **110**, 82–102.

ELLINGSEN, T. & PALM, E. 1975 Stability of linear flow. *Phys. Fluids* **18**, 487.

FARRELL, B. F. 1988 Optimal excitation of perturbations in viscous shear flow. *Phys. Fluids* **31**, 2093–2102.

FARRELL, B. F. & IOANNOU, P. J. 1993 Optimal excitation of three-dimensional perturbations in viscous constant shear flow. *Phys. Fluids* A **5**, 1390.

FISCHER, P. F., LOTTES, J. W. & KERKEMEIER, S. G. 2008 nek5000 web page. http://nek5000.mcs.anl.gov.

GALIONIS, I. & HALL, P. 2005 Spatial stability of the incompressible corner flow. *Theor. Comput. Fluid Dyn.* **19**, 77–113.

GHIA, K. N. 1975 Incompressible streamwise flow along an unbounded corner. *AIAA J.* **13**, 902–907.

GHIA, K. N. & DAVIS, R. T. 1974 A study of compressible potential and asymptotic viscous flows for corner region. *AIAA J.* **12**, 355–359.

KARP, M. & COHEN, J. 2014 Tracking stages of transition in Couette flow analytically. *J. Fluid Mech.* **748**, 896–931.

KORNILOV, V. I. & KHARITONOV, A. M. 1982 On the part played by the local pressure gradient in forming the flow in a corner. *Fluid Dyn.* **17**, 242–246.

LAKIN, W. D. & HUSSAINI, M. Y. 1984 Stability of the laminar boundary layer in a streamwise corner. *Proc. R. Soc. Lond.* A **393**, 101–116.

LANDAHL, M. T. 1975 Wave breakdown and turbulence. *SIAM J. Appl. Maths* **28** (4), 735–756.

LANDAHL, M. T. 1980 A note on an algebraic instability of inviscid parallel shear flows. *J. Fluid Mech.* **98** (02), 243–251.

LINDZEN, R. S. 1988 Instability of plane parallel shear flow (toward a mechanistic picture of how it works). *Pure Appl. Geophys.* **126** (1), 103–121.

LUCHINI, P. 2000 Reynolds-number-independent instability of the boundary layer over a flat surface: optimal perturbations. *J. Fluid Mech.* **404** (1), 289–309.

MACK, L. M.1984 Boundary-layer linear stability theory. AGARD Rep. No. 709.

MATLAB 2013 *Version 8.1.0.604 (R2013a)*. The MathWorks Inc.

MIKHAIL, A. G. & GHIA, K. N. 1978 Viscous compressible flow in the boundary region of an axial corner. *AIAA J.* **16**, 931–939.

MONOKROUSOS, A., ÅKERVIK, E., BRANDT, L. & HENNINGSON, D. S. 2010 Global three-dimensional optimal disturbances in the blasius boundary-layer flow using time-steppers. *J. Fluid Mech.* **650**, 181–214.

MONOKROUSOS, A., BOTTARO, A., BRANDT, L., DI VITA, A. & HENNINGSON, D. S. 2011 Nonequilibrium thermodynamics and the optimal path to turbulence in shear flows. *Phys. Rev. Lett.* **106** (13), 134502.

NOMURA, Y. 1962 Theoretical and experimental investigations on the incompressible viscous flow around the corner. *Memo Defence Acad. Japan* **2**, 115–145.

ORR, W. M. F. 1907 The stability or instability of the steady motions of a perfect liquid and of a viscous liquid. In *Proceedings of the Royal Irish Academy. Section A: Mathematical and Physical Sciences*, vol. 27. JSTOR.

PAL, A. & RUBIN, S. G. 1971 Asymptotic features of viscous flow along a corner. *Q. Appl. Maths* **29**, 91–108.

PARKER, S. J. & BALACHANDAR, S. 1999 Viscous and inviscid instabilities of flow along a streamwise corner. *Theor. Comput. Fluid Dyn.* **13**, 231–270.

PATERA, A. T. 1984 A spectral element method for fluid dynamics: laminar flow in a channel expansion. *J. Comput. Phys.* **54** (3), 468–488.

REDDY, S. C. & HENNINGSON, D. S. 1993 Energy growth in viscous channel flows. *J. Fluid Mech.* **252** (1), 209–238.

REDDY, S. C., SCHMID, P. J. & HENNINGSON, D. S. 1993 Pseudospectra of the Orr–Sommerfeld operator. *SIAM J. Appl. Maths* **53** (1), 15–47.

RIDHA, A. 1992 On the dual solutions associated with boundary-layer equations in a corner. *J. Engng Maths* **26**, 525–537.

RIDHA, A. 2003 Flow along streamwise corners revisited. *J. Fluid Mech.* **476**, 223–265.

RUBIN, S. G. 1966 Incompressible flow along a corner. *J. Fluid Mech. Digital Arch.* **26** (01), 97–110.

RUBIN, S. G. & GROSSMAN, B. 1971 Viscous flow along a corner: numerical solution of the corner layer equations. *Q. Appl. Maths* **29**, 169–186.

SCHMID, P. J. & HENNINGSON, D. S. 2001 *Stability and Transition in Shear Flows*. Springer.

SCHMIDT, O. T. & RIST, U. 2011 Linear stability of compressible flow in a streamwise corner. *J. Fluid Mech.* **688**, 569–590.

SCHMIDT, O. T. & RIST, U. 2014 Viscid–inviscid pseudo-resonance in streamwise corner flow. *J. Fluid Mech.* **743**, 327–357.

SIPP, D. & MARQUET, O. 2013 Characterization of noise amplifiers with global singular modes: the case of the leading-edge flat-plate boundary layer. *Theor. Comput. Fluid Dyn.* **27** (5), 617–635.

TANNEHILL, J., ANDERSON, D. & PLETCHER, R. 1997 *Computational Fluid Mechanics and Heat Transfer*. Taylor & Francis.

THEOFILIS, V. 2003 Advances in global linear instability analysis of nonparallel and three-dimensional flows. *Prog. Aerosp. Sci.* **39**, 249–315.

TREFETHEN, L. N. 1991 Pseudospectra of matrices. *Numer. Anal.* **91**, 234–266.

TREFETHEN, L. N., TREFETHEN, A. E., REDDY, S. C. & DRISCOLL, T. A. 1993 Hydrodynamic stability without eigenvalues. *Science* **261** (5121), 578–584.

WEINBERG, B. C. & RUBIN, S. G. 1972 Compressible corner flow. *J. Fluid Mech.* **56**, 753–774.

WRIGHT, T. G. 2002 Eigtool. http://www.comlab.ox.ac.uk/pseudospectra/eigtool/.

ZAMIR, M. 1981 Similarity and stability of the laminar boundary layer in a streamwise corner. *Proc. R. Soc. Lond.* A **377**, 269–288.

ZAMIR, M. & YOUNG, A. D. 1970 Experimental investigation of the boundary layer in a streamwise corner. *Aeronaut. Q.* **21**, 313–339.